Relativistic nuclear energy density functionals: Adjusting parameters to binding energies

T. Nikšić and D. Vretenar
Physics Department, Faculty of Science, University of Zagreb, HR-10000 Zagreb, Croatia

P. Ring
Physik-Department der Technischen Universität München, D-85748 Garching, Germany
(Received 19 May 2008; published 25 September 2008)

We study a particular class of relativistic nuclear energy density functionals in which only nucleon degrees of freedom are explicitly used in the construction of effective interaction terms. Short-distance (high-momentum) correlations, as well as intermediate- and long-range dynamics, are encoded in the medium (nucleon-density) dependence of the strength functionals of an effective interaction Lagrangian. Guided by the density dependence of microscopic nucleon self-energies in nuclear matter, a phenomenological ansatz for the density-dependent coupling functionals is accurately determined in self-consistent mean-field calculations of binding energies of a large set of axially deformed nuclei. The relationship between the nuclear matter volume, surface, and symmetry energies and the corresponding predictions for nuclear masses is analyzed in detail. The resulting best-fit parametrization of the nuclear energy density functional is further tested in calculations of properties of spherical and deformed medium-heavy and heavy nuclei, including binding energies, charge radii, deformation parameters, neutron skin thickness, and excitation energies of giant multipole resonances.

DOI: 10.1103/PhysRevC.78.034318 PACS number(s): 21.30.Fe, 21.60.Jz, 21.10.Dr, 21.10.Ft

I. INTRODUCTION

Among the microscopic approaches to the nuclear many-body problem, the framework of nuclear energy density functionals (NEDF) provides the most complete and accurate description of ground-state properties and collective excitations over the whole nuclide chart. Probably no other method achieves comparable accuracy at the same computational cost. At the level of practical applications the NEDF framework is realized in terms of self-consistent mean-field (SCMF) models based, for instance, on the Gogny effective interaction, the Skyrme energy functional, and the relativistic meson-exchange effective Lagrangian [1,2]. In the mean-field approximation the dynamics of the nuclear many-body system is represented by independent nucleons moving in self-consistent potentials, which correspond to the actual density and current distributions of a given nucleus.

The SCMF approach to nuclear structure is analogous to Kohn-Sham density functional theory [3,4], and nuclear mean-field models approximate the exact energy functional, which includes all higher order correlations, with powers and gradients of ground-state nucleon densities and currents [5]. In particular, a number of very successful relativistic mean-field (RMF) models have been constructed based on the framework of quantum hadrodynamics (QHD) [6,7]. There are important advantages in using functionals with manifest covariance [8]. The most obvious is the natural inclusion of the nucleon spin degree of freedom and the resulting nuclear spin-orbit potential that emerges automatically with the empirical strength in a covariant formulation. The consistent treatment of large, isoscalar, Lorentz scalar, and vector self-energies provides a unique parametrization of time-odd components of the nuclear mean-field (i.e., nucleon currents), which is absent in the nonrelativistic representation of the energy density functional. The empirical pseudospin symmetry in nuclear spectroscopy finds a natural explanation in terms of relativistic mean fields [9]. On a microscopic level, it has been argued [8] that a covariant formulation of nuclear dynamics manifests the true energy scales of QCD in nuclei and is consistent with the nonlinear realization of chiral symmetry through the implicit inclusion of pion-nucleon dynamics in the effective nucleon self-energies. A covariant treatment of nuclear matter provides a distinction between scalar and four-vector nucleon self energies, leading to a very natural saturation mechanism.

In conventional QHD the nucleus is described as a system of Dirac nucleons coupled to exchange mesons through an effective Lagrangian. The isoscalar-scalar σ meson, the isoscalar-vector ω meson, and the isovector-vector ρ meson build the minimal set of meson fields that is necessary for a description of bulk and single-particle nuclear properties. Of course, at the scale of low-energy nuclear structure, heavy-meson exchange is just a convenient representation of the effective nuclear interaction. At the energy and momentum scales characteristic of nuclei, the only degrees of freedom that have to be taken into account explicitly in the description of many-body dynamics are pions and nucleons. The behavior of the nucleon-nucleon (NN) interaction at long and intermediate distances is determined by one- and two-pion exchange processes. The exchange of heavy mesons is associated with short-distance dynamics that cannot be resolved at low energies that characterize nuclear binding and, therefore, can be represented by local four-point (contact) NN interactions, with low-energy (medium-dependent) parameters adjusted to nuclear data. These concepts of effective field theory and density functional theory methods have recently been used to derive a microscopic relativistic energy density functional framework constrained by in-medium QCD sum rules and chiral symmetry [10,11]. The density dependence of the effective nucleon-nucleon couplings is determined from

the long- and intermediate-range interactions generated by one- and two-pion exchange processes. They are computed by using in-medium chiral perturbation theory, explicitly including $\Delta(1232)$ degrees of freedom [12]. Regularization-dependent contributions to the energy density of nuclear matter, calculated at the three-loop level, are absorbed in contact interactions with parameters representing unresolved short-distance dynamics.

However, even in a fully microscopic approach that starts from a description of symmetric and asymmetric homogeneous and inhomogeneous nuclear matter, the parameters of a nuclear energy density functional still have to be fine-tuned to structure data of finite nuclei. This is simply because gross properties of infinite nuclear matter cannot determine the density functional on the level of accuracy that is needed for a quantitative description of structure phenomena in finite nuclei. For most functionals this tuning is performed on a relatively small set of spherical closed-shell nuclei, mainly because they are simple to calculate and can therefore be easily included in multiparameter *least-squares* fits. A problem arises, however, because ground-state data of closed-shell nuclei include long-range correlations that cannot really be absorbed into mean-field functionals. Generally, this will affect the predictive power of energy density functionals when they are used in the description of phenomena related to the evolution of shell structure. For instance, soft potential energy surfaces and/or small energy differences between coexisting minima in deformed nuclei are often difficult to describe by using functionals adjusted solely to data of spherical nuclei, even when sophisticated models are employed that include angular momentum and particle number projection, as well as intrinsic configuration mixing.

In this work we explore a class of relativistic energy density functionals originally introduced in Refs. [10,11] but, instead of using low-energy QCD constraints for the medium dependence of the parameters, a phenomenological ansatz is adjusted exclusively to masses of a relatively large set of axially deformed nuclei. The phenomenological approach, although guided by microscopic nucleon self-energies in nuclear matter, gives us more freedom to investigate in detail the relationship between global properties of a nuclear matter equation of state (volume, surface, and asymmetry energies) and the corresponding predictions for nuclear binding energies. Eventually, the goal will be to develop an energy density functional that does not implicitly contain symmetry breaking corrections and quadrupole fluctuation correlations and is therefore better suited for the new relativistic model that uses the generator coordinate method to perform configuration mixing of angular-momentum- and particle-number-projected relativistic wave functions [13,14]. The idea is that those correlations that we wish to treat explicitly should not be included in the density functional in an implicit way (i.e., by adjusting parameters to data that already include correlations). The solution could be to adjust the functional to pseudodata, obtained by subtracting correlation effects from experimental masses and, eventually, radii. This is most easily done by using masses of axially deformed nuclei with large deformation parameters, because the dominant contribution to their ground-state correlation energies is the rotational energy correction [15], which is relatively simple to calculate. Approximate methods for the calculation of correlations have been developed [16], enabling a systematic evaluation of correlation energies for the nuclear mass table. Of course one expects that the corresponding modifications of the parameters of the energy density functional will be relatively small, but even a small change in the relative contribution of various interaction terms could be the decisive factor in the description of soft potential energy surfaces, coexistence of prolate and oblate shapes, level ordering, etc. Very recent examples include the phenomenon of shape coexistence in neutron-deficient Kr isotopes [17,18] and the description of singular properties of excitation spectra and transition rates at critical points of quantum shape phase transitions [19]. As a first step toward the construction of a relativistic density functional that could provide a more accurate description of phenomena related to the evolution of shell structure, in this work we explore the possibility of determining the parameters of a given functional using only binding energies of axially deformed nuclei.

In Sec. II we construct the relativistic nuclear energy density functional based on these conjectures and discuss the necessary approximations and fitting strategies. In Sec. III, starting from microscopic nucleon self-energies in nuclear matter, and empirical global properties of the nuclear matter equation of state, we determine the functional accurately in a careful comparison of the predicted binding energies with data, for a set of 64 axially deformed nuclei in the mass regions $A \approx 150$–180 and $A \approx 230$–250. In Sec. IV the new energy density functional is thoroughly tested in a series of illustrative calculations of properties of spherical and deformed medium-heavy and heavy nuclei, including binding energies, charge radii, deformation parameters, neutron skin thickness, and excitation energies of giant multipole resonances. Section V summarizes the results of the present investigations and ends with an outlook for future studies.

II. RELATIVISTIC NUCLEAR ENERGY DENSITY FUNCTIONAL

The basic building blocks of a relativistic nuclear energy density functional are the densities and currents bilinear in the Dirac spinor field ψ of the nucleon:

$$\bar{\psi}\mathcal{O}_\tau\Gamma\psi, \quad \mathcal{O}_\tau \in \{1, \tau_i\}, \quad \Gamma \in \{1, \gamma_\mu, \gamma_5, \gamma_5\gamma_\mu, \sigma_{\mu\nu}\}. \tag{1}$$

Here τ_i are the isospin Pauli matrices and Γ generically denotes the Dirac matrices. The nuclear ground-state density and energy are determined by the self-consistent solution of relativistic linear single-nucleon Kohn-Sham equations. To derive those equations it is useful to construct an interaction Lagrangian with four-fermion (contact) interaction terms in the various isospace-space channels:

(i) isoscalar-scalar: $(\bar{\psi}\psi)^2$,
(ii) isoscalar-vector: $(\bar{\psi}\gamma_\mu\psi)(\bar{\psi}\gamma^\mu\psi)$,
(iii) isovector-scalar: $(\bar{\psi}\vec{\tau}\psi)\cdot(\bar{\psi}\vec{\tau}\psi)$, and
(iv) isovector-vector: $(\bar{\psi}\vec{\tau}\gamma_\mu\psi)\cdot(\bar{\psi}\vec{\tau}\gamma^\mu\psi)$.

Vectors in isospin space are denoted by arrows. A general Lagrangian can be written as a power series in the currents

$\bar{\psi}\mathcal{O}_\tau\Gamma\psi$ and their derivatives, with higher order terms representing in-medium many-body correlations [20–24]. We will adopt the approach of Refs. [10,11] and construct a Lagrangian with second-order interaction terms only, with many-body correlations encoded in density-dependent coupling functions. In complete analogy to the successful meson-exchange RMF phenomenology, in which the isoscalar-scalar σ meson, the isoscalar-vector ω meson, and the isovector-vector ρ meson build the minimal set of meson fields that is necessary for a description of bulk and single-particle nuclear properties, we consider an effective Lagrangian that includes the isoscalar-scalar, isoscalar-vector, and isovector-vector four-fermion interactions:

$$\begin{aligned}\mathcal{L} = {} & \bar{\psi}(i\gamma\cdot\partial - m)\psi \\ & - \frac{1}{2}\alpha_S(\hat{\rho})(\bar{\psi}\psi)(\bar{\psi}\psi) - \frac{1}{2}\alpha_V(\hat{\rho})(\bar{\psi}\gamma^\mu\psi)(\bar{\psi}\gamma_\mu\psi) \\ & - \frac{1}{2}\alpha_{TV}(\hat{\rho})(\bar{\psi}\vec{\tau}\gamma^\mu\psi)(\bar{\psi}\vec{\tau}\gamma_\mu\psi) \\ & - \frac{1}{2}\delta_S(\partial_\nu\bar{\psi}\psi)(\partial^\nu\bar{\psi}\psi) - e\bar{\psi}\gamma\cdot A\frac{(1-\tau_3)}{2}\psi. \end{aligned} \tag{2}$$

In addition to the free-nucleon Lagrangian and the point-coupling interaction terms, when applied to nuclei, the model must include the coupling of the protons to the electromagnetic field. The derivative term in Eq. (2) accounts for leading effects of finite-range interactions that are crucial for a quantitative description of nuclear density distribution (e.g., nuclear radii). Similar interactions can be included in each space-isospace channel, but in practice data on charge radii constrain only a single derivative term, for instance $\delta_S(\partial_\nu\bar{\psi}\psi)(\partial^\nu\bar{\psi}\psi)$. The coupling parameter δ_S has been estimated, for instance, from an in-medium chiral perturbation calculation of inhomogeneous nuclear matter [12]. In the region of nucleon densities relevant for the description of finite nuclei ($0.1 \leqslant \rho \leqslant 0.15\ \mathrm{fm}^{-3}$), the coupling strength of the derivative term displays a rather weak density dependence and can be approximated by a constant value δ_S between -0.85 and $-0.7\ \mathrm{fm}^4$. Note that the inclusion of an adjustable derivative term only in the isoscalar-scalar channel is consistent with conventional meson-exchange RMF models, in which the mass of the fictitious σ meson is adjusted to nuclear matter and ground-state properties of finite nuclei, whereas free values are used for the masses of the ω and ρ mesons.

The point-coupling Lagrangian [Eq. (2)] does not include isovector-scalar terms. In the meson-exchange picture this channel is represented by the exchange of an effective δ meson, and its inclusion introduces a proton-neutron effective mass splitting and enhances the isovector spin-orbit potential. However, in calculations of ground-state properties of finite nuclei, using both meson-exchange [25,26] and point-coupling [24] models, it has not been possible to constrain the parameters of the effective interaction in the isovector-scalar channel. Although the isovector strength has a relatively well-defined value, the distribution between the scalar and vector channels is not determined by ground-state data. To reduce the number of adjustable parameters, the isovector-scalar channel may be omitted from an energy density functional that will primarily be used for the description of low-energy nuclear structure.

The strength parameters of the interaction terms in Eq. (2) are functions of the nucleon four-current:

$$j^\mu = \bar{\psi}\gamma^\mu\psi = \hat{\rho}u^\mu, \tag{3}$$

where u^μ is the four-velocity defined as $(1-\boldsymbol{v}^2)^{-1/2}(1,\boldsymbol{v})$. In the rest frame of the nuclear system, $\boldsymbol{v}=0$. The single-nucleon Dirac equation, the relativistic analog of the Kohn-Sham equation, is obtained from the variation of the Lagrangian with respect to $\bar{\psi}$:

$$\left[\gamma_\mu\left(i\partial^\mu - \Sigma^\mu - \Sigma_R^\mu\right) - (m + \Sigma_S)\right]\psi = 0, \tag{4}$$

with the nucleon self-energies defined by the following relations:

$$\Sigma^\mu = \alpha_V(\rho_v)j^\mu + e\frac{(1-\tau_3)}{2}A^\mu, \tag{5}$$

$$\Sigma_R^\mu = \frac{1}{2}\frac{j^\mu}{\rho_v}\left\{\frac{\partial\alpha_S}{\partial\rho}\rho_s^2 + \frac{\partial\alpha_V}{\partial\rho}j_\mu j^\mu + \frac{\partial\alpha_{TV}}{\partial\rho}\vec{j}_\mu\vec{j}^\mu\right\}, \tag{6}$$

$$\Sigma_S = \alpha_S(\rho_v)\rho_s - \delta_S\Box\rho_s, \tag{7}$$

$$\Sigma_{TV}^\mu = \alpha_{TV}(\rho_v)\vec{j}^\mu. \tag{8}$$

In addition to the contributions of the isoscalar-vector four-fermion interaction and the electromagnetic interaction, the isoscalar-vector self-energy Σ^μ includes the "rearrangement" terms Σ_R^μ, arising from the variation of the vertex functionals α_S, α_V, and α_{TV} with respect to the nucleon fields in the density operator $\hat{\rho}$. The inclusion of the rearrangement self-energy is essential for energy-momentum conservation and the thermodynamical consistency of the model [26–28]. Σ_S and Σ_{TV}^μ denote the isoscalar-scalar and isovector-vector self-energies, respectively.

In the relativistic density functional framework the nuclear ground state $|\phi_0\rangle$ is represented by the mean-field self-consistent solution of the system of Eqs. (4)–(8), with the isoscalar and isovector four-currents and scalar density

$$j_\mu = \langle\phi_0|\bar{\psi}\gamma_\mu\psi|\phi_0\rangle = \sum_{k=1}^{N} v_k^2\bar{\psi}_k\gamma_\mu\psi_k, \tag{9}$$

$$\vec{j}_\mu = \langle\phi_0|\bar{\psi}\gamma_\mu\vec{\tau}\psi|\phi_0\rangle = \sum_{k=1}^{N} v_k^2\bar{\psi}_k\gamma_\mu\vec{\tau}\psi_k, \tag{10}$$

$$\rho_S = \langle\phi_0|\bar{\psi}\psi|\phi_0\rangle = \sum_{k=1}^{N} v_k^2\bar{\psi}_k\psi_k, \tag{11}$$

where ψ_k are Dirac spinors, and the sum runs over occupied positive-energy single-nucleon orbitals, including the corresponding occupation factors v_k^2. The single-nucleon Dirac equations are solved self-consistently in the "no-sea" approximation that omits the explicit contribution of negative-energy solutions of the relativistic equations to the densities and currents. Vacuum polarization effects are implicitly included in the adjustable density-dependent parameters of the theory.

A large part of this work will be devoted to adjusting the free parameters of the medium-dependent point-coupling functionals α_S, α_V, and α_{TV} and the strength δ_S of the derivative term. To establish the density dependence of the couplings one could start from a microscopic (relativistic) equation of state (EoS) of symmetric and asymmetric nuclear

matter and map the corresponding nucleon self-energies on the mean-field self-energies [Eqs. (5)–(8)] that determine the single-nucleon Dirac equation [Eq. (4)]. This approach has been adopted, for instance, in RMF models based on Dirac-Brueckner-Hartree-Fock self-energies in nuclear matter [25,28,29] or on in-medium chiral perturbation theory (ChPT) calculations of the nuclear matter EoS [10,11]. In general, however, energy density functionals determined directly from a microscopic EoS do not provide a very accurate description of data in finite nuclei. The reason for this, of course, is that a calculation of the nuclear matter EoS involves approximation schemes and includes adjustable parameters that are not really constrained by nuclear structure data. The resulting bulk properties of infinite nuclear matter (saturation density, binding energy, compression modulus, and asymmetry energy) do not determine uniquely the parameters of nuclear energy density functionals, which usually must be further fine-tuned to ground-state data (masses and/or charge radii) of spherical nuclei.

In a phenomenological construction of a relativistic energy density functional one starts from an assumed ansatz for the medium dependence of the mean-field nucleon self-energies and adjusts the parameters directly to data of spherical nuclei. This procedure was used, for instance, in the construction of the relativistic density-dependent interactions TW-99 [26], DD-ME1 [27], DD-ME2 [30], PKDD [31], and PK01 [32].

This work adopts a different strategy and determines the parameters of the point-coupling Lagrangian [Eq. (2)] exclusively from a large data set of binding energies E_B of deformed nuclei. First one notes that calculated masses of finite nuclei are primarily sensitive to the three leading terms in the empirical mass formula (volume, surface, and symmetry energies):

$$E_B = a_v A + a_s A^{2/3} + a_4 \frac{(N-Z)^2}{4A} + \cdots. \qquad (12)$$

Therefore one can generate families of effective interactions that are characterized by different values of a_v, a_s and a_4 and determine which parametrization minimizes the deviation from the empirical binding energies of a large set of deformed nuclei. This approach differs considerably from the standard procedure of fitting parameters of nonrelativistic Skyrme or RMF functionals, in which a given set of parameters is adjusted simultaneously to a favorite nuclear matter EoS and to ground-state properties of about 10 spherical closed-shell nuclei. Deformed systems have generally not been included in fits of parameters of self-consistent RMF models, mainly because calculation of deformed nuclei is computationally more demanding and requires advanced computer codes. In this work parameters of relativistic energy density functionals are for the first time directly adjusted to binding energies of axially deformed nuclei in the mass regions $A \approx 150$–180 and $A \approx 230$–250.

To determine the functional form of the density dependence of the couplings α_S, α_V, and α_{TV}, one can start from microscopic nucleon self-energies in nuclear matter. In a recent analysis of relativistic nuclear dynamics [33], modern high-precision NN potentials (Argonne V_{18}, Bonn A, CD-Bonn, Idaho, Nijmegen, and $V_{\text{low }k}$) were mapped on a relativistic operator basis, and the corresponding relativistic nucleon self-energies in nuclear matter were calculated in a Hartree-Fock approximation at *tree level*. A very interesting result is that, at moderate nucleon densities relevant for nuclear structure calculations, all potentials yield very similar scalar and vector mean fields of several hundred MeV magnitude, in remarkable agreement with standard RMF phenomenology, giving at saturation density a large and attractive scalar field $\Sigma_s \approx -400$ MeV and a repulsive vector field $\Sigma_v \approx 350$ MeV. The different treatment of short-distance dynamics in the various NN potentials leads to slightly more pronounced differences between the corresponding self-energies at higher nucleon densities. Generally, however, all potentials predict a very similar density dependence of the scalar and vector self-energies. In the chiral effective field theory framework, in particular, these self-energies are predominantly generated by contact terms that occur at next-to-leading order in the chiral expansion.

Of course at the Hartree-Fock *tree level* these NN potentials do not yield saturation of nuclear matter. Nevertheless, the corresponding self-energies can be used as the starting point in the modeling of medium dependence of a relativistic nuclear energy density functional. Guided by the microscopic density dependence of the vector and scalar self-energies, we choose the following practical ansatz for the functional form of the couplings:

$$\alpha_i(\rho) = a_i + (b_i + c_i x)e^{-d_i x} (i \equiv S, V, TV), \qquad (13)$$

with $x = \rho/\rho_{\text{sat}}$, where ρ_{sat} denotes the nucleon density at saturation in symmetric nuclear matter. Note that the corresponding self-energies are defined in Eqs. (5)–(8). In the next section we will adjust the parameters of this ansatz simultaneously to infinite and semi-infinite nuclear matter and to binding energies of deformed nuclei. The resulting self-energies in nuclear matter will eventually be compared to our starting approximation: the Hartree-Fock scalar and vector self-energies of the Idaho next-to-next-to-next-to-leading order (N^3LO) potential [34].

In the isovector channel the corresponding Hartree-Fock *tree-level* nucleon self-energies, obtained by directly mapping microscopic NN potentials on a relativistic operator basis, are presently not available. Therefore, as was done in the case of the finite-range meson-exchange interactions TW-99 [26], DD-ME1 [27], DD-ME2 [30], and PK01 [32], the density dependence of the isovector-vector coupling function is determined from the results of Dirac-Brueckner calculations of asymmetric nuclear matter [29]. Accordingly, in Eq. (13) for the isovector channel we set two parameters to zero—$a_{TV} = 0$ and $c_{TV} = 0$—and adjust b_{TV} and d_{TV} to empirical properties of asymmetric matter and to nuclear masses, together with the parameters of the isoscalar channel.

III. THE EFFECTIVE DENSITY-DEPENDENT INTERACTION DD-PC1

A. Infinite and semi-infinite nuclear matter

The usual procedure in the construction of an effective mean-field interaction is the *least-squares* adjustment of

parameters to both nuclear matter EoS and to ground-state data (masses and charge radii) of spherical nuclei. Instead we generate sets of effective interactions with different values of the volume energy a_v, surface energy a_s, and symmetry energy a_4 in nuclear matter and analyze the corresponding binding energies of deformed nuclei with $A \approx 150$–180 and $A \approx 230$–250. The nuclear matter saturation density, compression modulus, and Dirac mass will be kept fixed throughout this analysis. The calculated binding energies of finite nuclei are not very sensitive to the nuclear matter saturation density, and we take $\rho_{\rm sat} = 0.152\,{\rm fm}^{-3}$, in accordance with values predicted by most modern relativistic mean-field models. In particular, this value has also been used for the meson-exchange effective interactions DD-ME1 [27] and DD-ME2 [30]. From these interactions we also take the Dirac effective nucleon mass $m^*_D = m + \Sigma_S = 0.58m$. In RMF theory the Dirac mass is closely related to the effective spin-orbit single-nucleon potential, and empirical energy spacings between spin-orbit partner states in finite nuclei determine a relatively narrow interval of allowed values: $0.57 \leqslant m^*_D/m \leqslant 0.61$. In a recent study [35] of the relation between finite-range (meson-exchange) and zero-range (point-coupling) representations of effective RMF interactions we have shown that, to reproduce experimental excitation energies of isoscalar giant monopole resonances, point-coupling interactions require a nuclear matter compression modulus $K_{\rm nm} \approx 230$ MeV, considerably lower than values typically used for finite-range meson-exchange relativistic interactions. Thus we take $K_{\rm nm} = 230$ MeV for all effective interactions considered in the present analysis.

Of course if only nuclear matter properties at the point of saturation density were specified, one could parametrize a number of realistic effective interactions that would be difficult to compare at the level of finite nuclei. In particular, nuclear structure data do not constrain the nuclear matter EoS at high nucleon densities. Therefore, in addition to $\rho_{\rm sat}$, m^*_D, and $K_{\rm nm}$, we fix two additional points on the $E(\rho)$ curve in symmetric matter to the microscopic EoS of Akmal, Pandharipande, and Ravenhall [36], based on the Argonne $V_{18}NN$ potential and the UIX three-nucleon interaction. This EoS has extensively been used in studies of high-density nucleon matter and neutron stars. At almost four times nuclear matter saturation density, we choose the point $\rho = 0.56\,{\rm fm}^{-3}$ with $E/A = 34.39$ MeV and, to have an overall consistency, one point at low density: $\rho = 0.04\,{\rm fm}^{-3}$ with $E/A = -6.48$ MeV (cf. Table VI of Ref. [36]). As we have already emphasized in the previous section, by adjusting mean-field interactions exclusively to a microscopic EoS such as, for instance, the one calculated in Ref. [36], it is not possible to obtain a very accurate description of nuclear structure. Ground-state nuclear data must be used to fine-tune the parameters of effective interactions.

In contrast to the Dirac mass and saturation density, the nuclear matter volume energy coefficient a_v has a decisive influence on the calculated binding energies of finite nuclei. By using the framework of nonrelativistic Skyrme functionals, it was recently shown that even a relatively small change in the volume energy ($\approx 0.5\%$) can have a pronounced effect on the calculated masses of heavy and superheavy nuclei, as compared with experimental values [15,37]. In the framework of RMF models no attempt has been made so far to

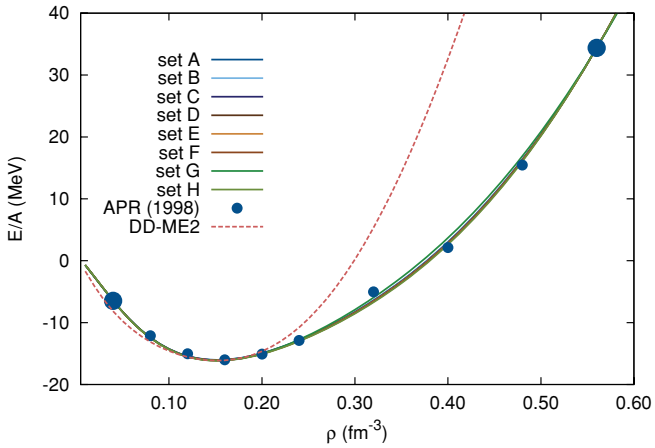

FIG. 1. (Color online) The equations of state of symmetric nuclear matter (binding energy as a function of nucleon density) for the eight point-coupling effective interactions of Table I, in comparison with the EoS of the meson-exchange effective interaction DD-ME2 [30] and the microscopic EoS of Ref. [36]. The two points from the microscopic EoS on which the point-coupling effective interactions (sets A–H) were adjusted are denoted by larger filled circle symbols.

constrain the value of volume energy better than the interval $-16.2 \leqslant a_v \leqslant -16$ MeV. To study in more detail the effect of volume energy on masses, we have generated point-coupling effective interactions characterized by the following values of the coefficient: $a_v = -16.02$ MeV (set A), $a_v = -16.04$ MeV (set B), $a_v = -16.06$ MeV (set C), $a_v = -16.08$ MeV (set D), $a_v = -16.10$ MeV (set E), $a_v = -16.12$ MeV (set F), $a_v = -16.14$ MeV (set G), and $a_v = -16.16$ MeV (set H). The corresponding parameters of the ansatz [Eq. (13)] for the functional form of the isoscalar couplings are collected in Table I. Note that to reduce the number of free parameters, we have set the value $c_V = 0$. The resulting binding energy curves for symmetric nuclear matter are plotted in Fig. 1, together with the EoS of the meson-exchange effective interaction DD-ME2 and the microscopic EoS of Ref. [36]. The two points on the microscopic EoS that have been used to adjust the parameters are represented by large filled circle symbols. Because of the anchor at $\rho = 0.56\,{\rm fm}^{-3}$, the new binding energy curves are, of course, different from DD-ME2 and much closer to the microscopic EoS. However, the high-density behavior has little influence on the description of low-energy nuclear structure data.

The isovector channel of the energy density functional determines the density dependence of the nuclear matter symmetry energy

$$S_2(\rho) = a_4 + \frac{p_0}{\rho^2_{\rm sat}}(\rho - \rho_{\rm sat}) + \frac{\Delta K_0}{18\rho^2_{\rm sat}}(\rho - \rho_{\rm sat})^2 + \cdots . \quad (14)$$

The parameter p_0 characterizes the linear density dependence of the symmetry energy, and ΔK_0 is the isovector correction to the compression modulus. Experimental masses, unfortunately, do not place very strict constraints on the parameters of the expansion of $S_2(\rho)$ [38], but self-consistent mean-field calculations show that binding energies can restrict the values of S_2 at nucleon densities somewhat below saturation

TABLE I. Isoscalar parameters [Eq. (13)] of the point-coupling effective interactions with volume energy coefficients $a_v = -16.02$ MeV (set A), $a_v = -16.04$ MeV (set B), $a_v = -16.06$ MeV (set C), $a_v = -16.08$ MeV (set D), $a_v = -16.10$ MeV (set E), $a_v = -16.12$ MeV (set F), $a_v = -16.14$ MeV (set G), and $a_v = -16.16$ MeV (set H).

Parameter	Set A	Set B	Set C	Set D	Set E	Set F	Set G	Set H
a_S (fm^2)	−10.0220	−10.0332	−10.0462	−10.0855	−10.0951	−10.1051	−10.1137	−10.1220
b_S (fm^2)	−9.1781	−9.1666	−9.1504	−9.0623	−9.0539	−9.0436	−9.0384	−9.0307
c_S (fm^2)	−6.2799	−6.3541	−6.4273	−6.4878	−6.5611	−6.6336	−6.7065	−6.7786
d_S	1.3585	1.3654	1.3724	1.3806	1.3872	1.3938	1.4001	1.4065
a_V (fm^2)	5.9020	5.9108	5.9195	5.9262	5.9348	5.9431	5.9513	5.9594
b_V (fm^2)	8.8711	8.8687	8.8637	8.8156	8.8150	8.8134	8.8148	8.8147
c_V (fm^2)	0.0	0.0	0.0	0.0	0.0	0.0	0.0	0.0
d_V	0.6548	0.65676	0.6584	0.6547	0.6568	0.6587	0.6610	0.6630

density (i.e., at $\rho \approx 0.1$ fm^{-3}). Additional information on the symmetry energy can be obtained from data on neutron skin thickness and excitation energies of giant dipole resonances. Although values of neutron radii are available only for a small number of nuclei and the corresponding uncertainties are large, recent studies have shown that relativistic effective interactions with volume asymmetry a_4 in the range $31 \leqslant a_4 \leqslant 35$ MeV predict values for neutron skin thickness that are consistent with data and reproduce experimental excitation energies of isovector giant dipole resonances (cf. Ref. [39] and references therein cited). Therefore we keep the volume asymmetry fixed at $a_4 = 33$ MeV and vary the symmetry energy at a density that corresponds to an average nucleon density in finite nuclei: $\langle\rho\rangle = 0.12$ fm^{-3}. The quantity $S_2(\rho = 0.12$ fm$^{-3})$ will be denoted $\langle S_2\rangle$.

Calculated binding energies and charge radii are strongly influenced by the choice of the surface energy coefficient a_s. In the present model the value of this quantity is determined by the strength δ_S of the derivative coupling term in the point-coupling Lagrangian [Eq. (2)]. For each effective interaction (sets A–H), we have calculated the surface energy and surface thickness of semi-infinite nuclear matter [40], for several values of the parameter δ_s in the range $-0.76 \leqslant \delta_S \leqslant -0.86$ fm^4. In Fig. 2 we plot the corresponding surface energies as functions of the surface thickness, in comparison to the point obtained with the finite-range interaction DD-ME2 ($t = 2.108$ fm, $a_s = 17.72$ MeV). Considering that DD-ME2 has an rms error of only 0.017 fm when compared to data on absolute charge radii and charge isotope shifts [30], and also taking into account the comparison between DD-ME2 and point-coupling RMF interactions of Ref. [35], we can deduce the following range for the parameter of the derivative coupling term: $-0.80 \geqslant \delta_S \geqslant -0.84$ fm^4, which is in very good agreement with the microscopic estimate of Ref. [12] for the region of nucleon densities $\rho \approx 0.1$ fm^3.

B. Deformed nuclei

If an effective interaction is adjusted to masses of finite nuclei by varying the volume, symmetry, and surface energies, the parameters of the energy density functional that determine these quantities will generally be correlated because of Eq. (14). When only a small number of nuclei is considered, satisfactory results can be obtained with various, in general linearly dependent, combinations of parameters. The new effective point-coupling interactions will therefore be analyzed on a set of 64 deformed nuclei, listed in Table II. To resolve the surface and volume contributions to binding energy, nuclides with mass number ranging from 154 to 250 are considered. The variation of the asymmetry coefficient

$$\alpha^2 = \frac{(N-Z)^2}{A^2} \tag{15}$$

in the range from 0.018 to 0.054 should suffice to deduce the isovector parameters that govern the symmetry energy contribution. The effect of shell closure is minimized by taking into account only well-deformed nuclei. Pairing correlations are treated in the BCS approximation with empirical pairing gaps (five-point formula). The pairing model space includes two major oscillator shells ($2\hbar\omega_0$) above the Fermi surface. The self-consistent single-nucleon RMF equations are solved by expanding nucleon spinors in terms of eigenfunctions of a deformed, axially symmetric harmonic oscillator potential [41]. In this work calculations of nuclear ground states are performed in a large basis of 16 major oscillator shells, and

TABLE II. The binding energies of the isotopic chains $62 \leqslant Z \leqslant 72$ and $90 \leqslant Z \leqslant 98$ have been used to adjust the parameters of relativistic point-coupling effective interactions. $N_{\min}$ and $N_{\max}$ denote the corresponding ranges of neutron number in even-even nuclides.

Z	62	64	66	68	70	72	90	92	94	96	98
$N_{\min}$	92	92	92	92	92	72	140	138	138	142	144
$N_{\max}$	96	98	102	104	108	110	144	148	150	152	152

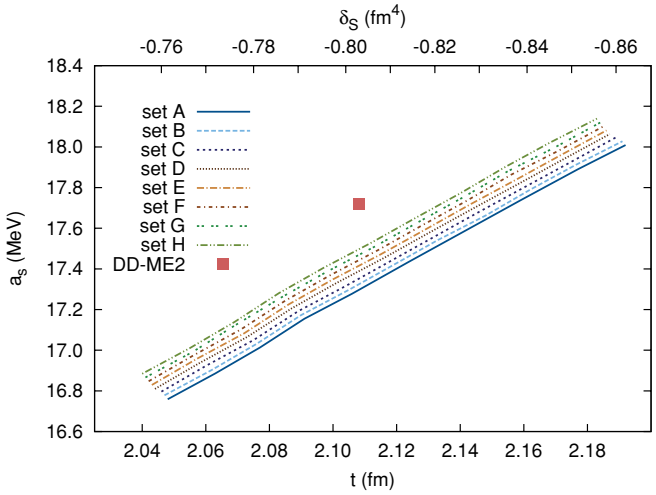

FIG. 2. (Color online) Surface energy of semi-infinite nuclear matter as a function of the surface thickness, for the eight point-coupling effective interactions of Table I. The corresponding values of the strength δ_S of the derivative coupling term in the point-coupling Lagrangian [Eq. (2)] are displayed on the upper horizontal axis. The filled square symbol denotes the surface energy and surface thickness predicted by the meson-exchange effective interaction DD-ME2 [30].

convergence has been tested in several calculations with 18 oscillator shells. After the self-consistent equations are solved, the microscopic estimate for the center-of-mass correction is subtracted from the total binding energy

$$E_{\text{c.m.}} = -\frac{\langle P^2_{\text{c.m.}} \rangle}{2Am}, \tag{16}$$

where $P_{\text{c.m.}}$ is the total momentum of a nucleus with A nucleons.

For each effective interaction with given volume energy a_v (sets A–H), and for six values of the symmetry energy $\langle S_2 \rangle = 27.6, 27.8, 28.0, 28.2, 28.4$, and 28.6 MeV, we have adjusted the surface energy [i.e., the coupling strength δ_S of the derivative term in the Lagrangian Eq. (2)] to a value that minimizes the deviation of the calculated binding energies from data for the set of nuclei listed in Table II. The required accuracy is 0.05%, which approximately corresponds to an absolute error of ± 1 MeV for the total binding energy. The resulting surface energies are plotted in Fig. 3 as functions of the volume energy, for each value of the symmetry energy $\langle S_2 \rangle$. At this point we have a set of 48 parametrizations of the energy density functional. Figure 4 displays the corresponding χ^2 values

$$\chi^2 = \sum_i \left(\frac{E_B^{\text{th}}(i) - E_B^{\text{exp}}(i)}{\Delta E_B^{\text{exp}}(i)} \right)^2, \tag{17}$$

where $E_B^{\text{exp}}(i)$ denote experimental binding energies [42], $E_B^{\text{th}}(i)$ are the corresponding theoretical values, $\Delta E_B^{\text{exp}}(i) = 0.0005 E_B^{\text{exp}}(i)$, and the sum runs over the set of 64 deformed nuclei. Although the span of χ^2 values is very large, the functional dependence of χ^2 on a_v is smooth and, for each value $\langle S_2 \rangle$ of the symmetry energy, there is a unique combination of volume and surface energies that minimizes χ^2. The minima of each curve are collected in Fig. 5. Also in this plot, χ^2 versus a_v displays a smooth parabola, with the absolute minimum at the point $a_v = -16.06$ MeV, $\langle S_2 \rangle = 27.8$ MeV, and $a_s = 17.498$ MeV. The χ^2 values of the neighboring points are not much larger, but obviously the systematics of binding energies excludes effective interactions with $a_v \leqslant -16.10$ MeV.

This result is illustrated in much more detail in Figs. 6–11, where we display the absolute deviations of the calculated binding energies from the experimental values for the effective interactions that correspond to each of the points included in Fig. 5. Because these interactions have already been optimized with respect to a_s (cf. Fig. 3) and $\langle S_2 \rangle$ (cf. Fig. 4), Figs. 6–11 show the isospin asymmetry (α^2) and mass dependencies of the absolute errors of calculated binding energies as functions of volume energy at saturation, a_v. Positive deviations correspond to underbound nuclei. We notice that not only does the interaction with $a_v = -16.06$ MeV (cf. Fig. 7) correspond

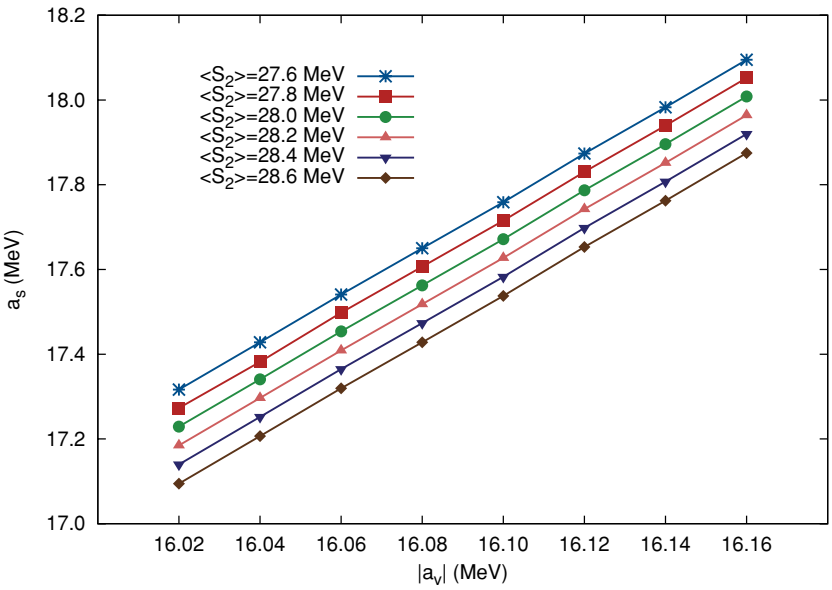

FIG. 3. (Color online) Surface energies of semi-infinite nuclear matter that minimize the deviation of the calculated binding energies from data, for the set of nuclei listed in Table II, plotted as functions of the volume energy at saturation, for six values of the symmetry energy $\langle S_2 \rangle$.

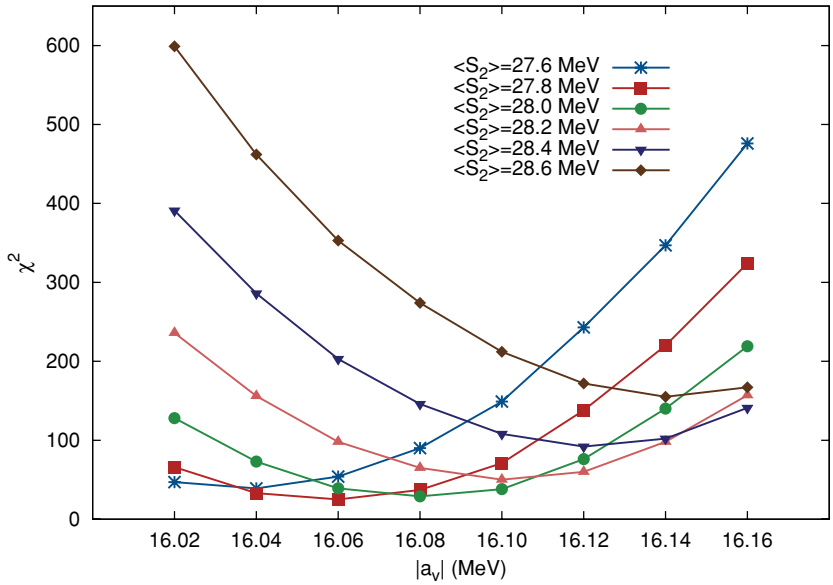

FIG. 4. (Color online) χ^2 deviations [Eq. (17)] of the theoretical binding energies from data for the set of deformed nuclei listed in Table II and for each combination of the surface, volume, and symmetry energy shown in Fig. 3.

to the lowest χ^2 value but also that it is the only one that does not display any visible isotopic or mass dependence of the deviations of calculated masses. The absolute errors for all 64 axially deformed nuclei in the mass regions $A \approx 150$–180 and $A \approx 230$–250 are smaller than 1 MeV. With stronger binding in symmetric nuclear matter (i.e., by increasing the absolute value of a_v), the corresponding deviations of calculated binding energies become larger, and they also acquire a definite isotopic dependence (cf. Figs. 8–11). Reducing the absolute value of a_v reverses the isotopic trend of the errors (cf. Fig. 6). The isospin and mass dependence of binding energies shown in Figs. 6–11 is one of the main results of the present analysis, and it illustrates the sensitivity of the calculated masses to the choice of the nuclear matter binding energy at saturation. It also clearly shows why it is not possible to accurately determine the parameters of a nuclear energy density functional already at nuclear matter level (i.e., in an *ab initio* approach starting from empirical NN and NNN interactions) without additional adjustment to low-energy data on finite medium-heavy and heavy nuclei.

The results of Figs. 6–11 can be compared to those obtained with one of the most successful finite-range meson-exchange

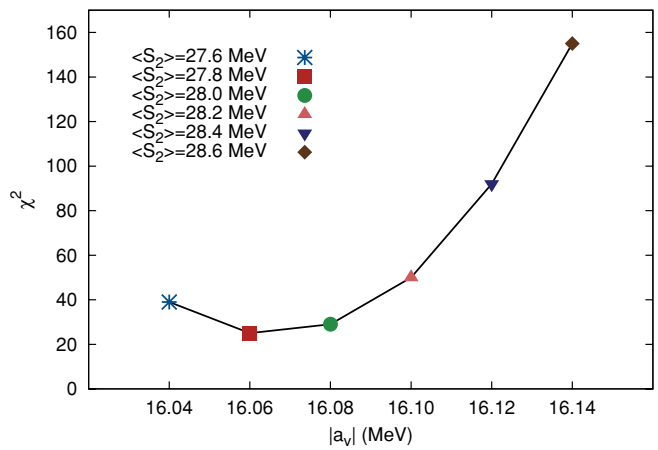

FIG. 5. (Color online) The minimum χ^2 deviation of the theoretical binding energies from data, as a function of the volume energy coefficient. Each point represents the minimum of the corresponding curve plotted in Fig. 4.

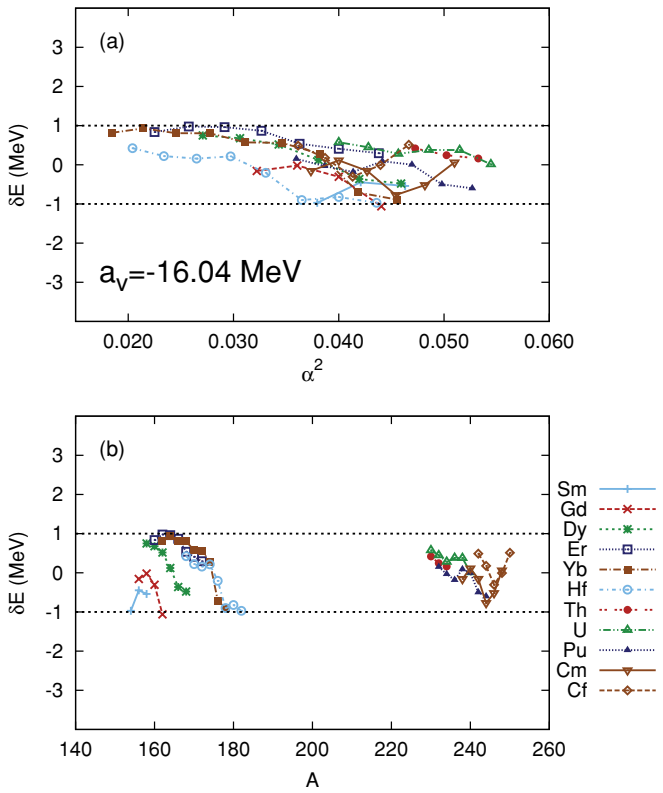

FIG. 6. (Color online) Absolute deviations of the calculated binding energies from the experimental values of the 64 axially deformed nuclei listed in Table II, as functions of (a) the asymmetry coefficient and (b) the mass number. Lines connect nuclei that belong to the isotopic chains shown in the legend. The theoretical binding energies are calculated by using the point-coupling effective interaction characterized by the volume energy $a_v = -16.04$ MeV.

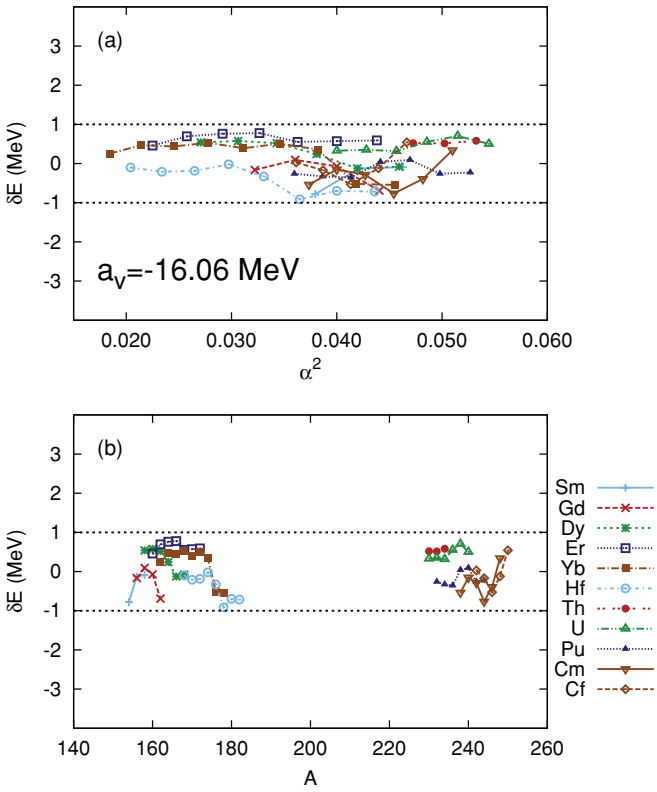

FIG. 7. (Color online) Same as in Fig. 6, but for the point-coupling effective interaction with volume energy $a_v = -16.06$ MeV.

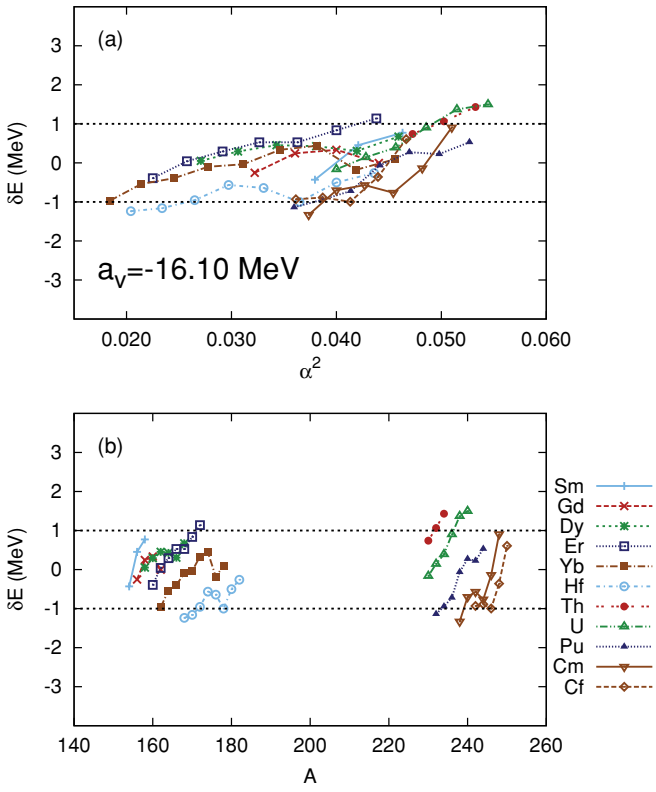

FIG. 9. (Color online) Same as in Fig. 6, but for the point-coupling effective interaction with volume energy $a_v = -16.10$ MeV.

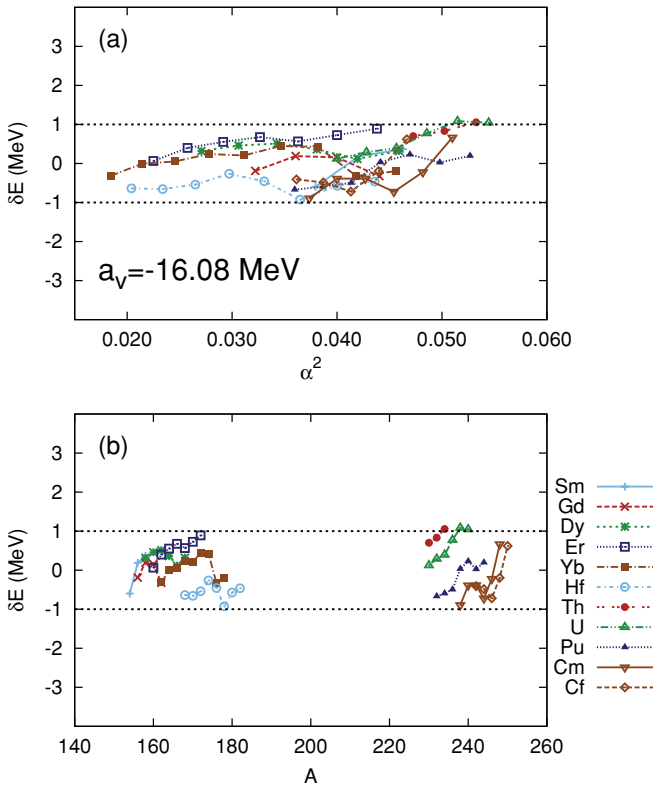

FIG. 8. (Color online) Same as in Fig. 6, but for the point-coupling effective interaction with volume energy $a_v = -16.08$ MeV.

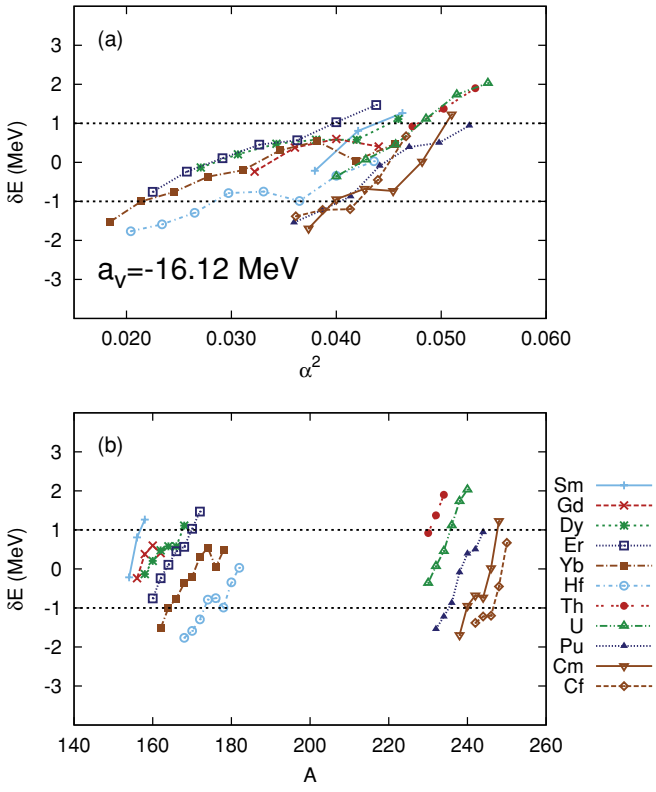

FIG. 10. (Color online) Same as in Fig. 6, but for the point-coupling effective interaction with volume energy $a_v = -16.12$ MeV.

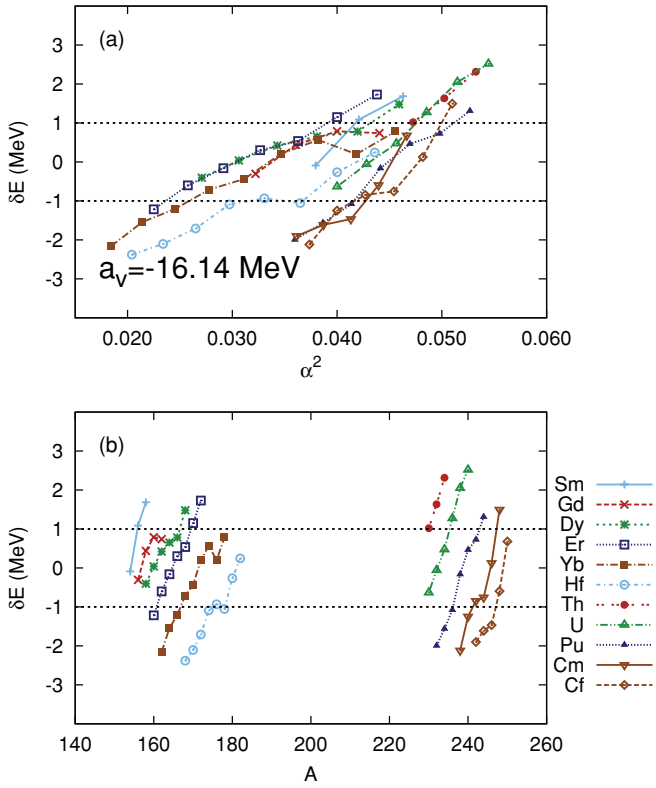

FIG. 11. (Color online) Same as in Fig. 6, but for the point-coupling effective interaction with volume energy $a_v = -16.14$ MeV.

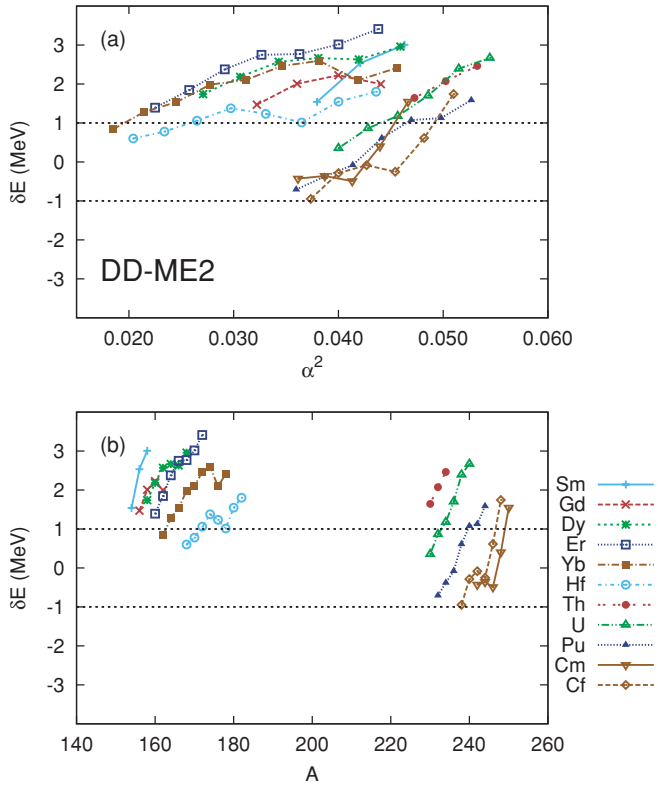

FIG. 12. (Color online) Absolute deviations of the calculated binding energies from the experimental values of the 64 axially deformed nuclei listed in Table II, as functions of (a) the asymmetry coefficient and (b) the mass number. Lines connect nuclei that belong to the isotopic chains shown in the legend. The theoretical binding energies are calculated by using the meson-exchange effective interaction DD-ME2 [30].

effective interactions: DD-ME2 (cf. Fig. 12). The volume energy coefficient of DD-ME2 is $a_v = -16.14$ MeV, and the parameters were adjusted to binding energies, charge radii, and neutron radii of 12 spherical nuclei [30]. One notices both the pronounced isotopic and mass dependence of the deviations of binding energies calculated with DD-ME2. Although the span of the DD-ME2 absolute errors is somewhat smaller than that of the corresponding point-coupling effective interaction with $a_v = -16.14$ MeV (cf. Fig. 11), the meson-exchange interaction obviously underbinds most of the 64 axially deformed nuclei, especially in the mass region $A \approx 150$–180. This is because DD-ME2 was adjusted to binding energies of spherical nuclei, and therefore it implicitly includes closed-shell effects beyond the mean field. Virtually all self-consistent relativistic models based on the static mean-field approximation are characterized by relatively small effective nucleon masses, because in the RMF framework the nonrelativistic-type effective mass $m^*_{\rm NR}$ [43] is not independent of the Dirac mass $m^*_D = m - \Sigma_S$. The latter determines not only the nucleon spin-orbit potential but also the binding of symmetric nuclear matter and, therefore, constraints the nonrelativistic-type effective mass to a rather narrow interval around $m^*_{\rm NR} \approx 0.65m$. A small effective mass translates into low density of single-nucleon states around the Fermi surface. This is especially pronounced in magic nuclei where standard RMF models predict much too large energy gaps between occupied and unoccupied major shells. When these interactions are nevertheless forced to reproduce experimental binding energies of magic nuclei (i.e., when their parameters are adjusted to masses of nuclei such as ^{132}Sn and ^{208}Pb), the surrounding open-shell nuclei are predicted to be underbound, giving rise to characteristic "arches" of the deviations between theoretical and experimental binding energies [15,30]. Arches between shell closures (i.e., the overbinding of closed-shell nuclei relative to surrounding open-shell nuclei) characterize also most nonrelativistic self-consistent mean-field models (e.g., Skyrme-type effective interactions [15]).

It has become customary to adjust nonrelativistic and relativistic energy density functionals to ground-state data of magic, closed-shell nuclei. However, the resulting effective interactions are rarely used to calculate low-lying spectra of spherical nuclei. These functionals are more successful in the description of the evolution of deformation, shape coexistence phenomena, rotational bands, etc. in deformed nuclei. This is the rationale behind the present adjustment of the relativistic energy density functional directly to masses of axially deformed medium-heavy and heavy nuclei. This procedure, of course, does not solve the problem of arches. They are still present, but now magic, closed-shell nuclei are overbound with respect to experimental binding energies.

In this section it has been shown that, among the effective density-dependent point-coupling interactions considered in

the present analysis, the one with volume energy $a_v = -16.06$ MeV, surface energy $a_s = 17.498$ MeV, and symmetry energy $\langle S_2 \rangle = 27.8$ MeV ($a_4 = 33$ MeV) yields best results for the binding energies of axially deformed nuclei in the mass regions $A \approx 150$–180 and $A \approx 230$–250. We will denote this interaction DD-PC1 (density-dependent point-coupling). In addition to the parameters of the isoscalar terms (set C in Table I) and the strength of the derivative term $\delta_S = -0.815$ fm^4, DD-PC1 is completely specified by the two parameters of the isovector channel: $b_{TV} = 1.836$ fm^2 and $d_{TV} = 0.64$. The total number of parameters is 10. In the next section a number of calculations will be performed that illustrate not only the predictive power of DD-PC1 but also problems in the calculation of masses of spherical nuclei.

Finally, in Fig. 13 we compare the density dependence of the DD-PC1 isoscalar vector and scalar nucleon self-energies in symmetric nuclear matter with the starting approximation given by the Hartree-Fock (HF) self-energies [33] calculated from the Idaho N^{3}LO NN potential [34]. As already emphasized, the analysis of Ref. [33] has shown that at the relativistic HF level microscopic NN potentials do not yield nuclear matter saturation. To achieve saturation of homogeneous symmetric matter, and to reproduce binding energies of finite nuclei, the self-consistent DD-PC1 mean fields must include effects of short-range correlations. This necessitates an increase in magnitude of the HF scalar self-energy for nucleon densities below $2\rho_{\rm sat}$. At saturation density, in particular, this increase is 70 MeV and we also note the pronounced exponential dependence on density of the DD-PC1 self-energies, as compared to the almost linear density dependence of the HF Idaho self-energies. The magnitude of the scalar self-energy also determines the effective Dirac mass and, therefore, the strength of the effective nucleon spin-orbit potential in finite nuclei. At low densities below $\rho_{\rm sat}$ the HF Idaho vector self-energy is much less modified by the requirement of saturation and self-consistency. An interesting result is that, at saturation density, the HF Idaho and DD-PC1 vector self-energies differ by less than 3 MeV. At much higher nucleon densities the behavior of the DD-PC1 self-energies has been determined by fixing the EoS to the point $\rho = 0.56\,\text{fm}^{-3}$ on the microscopic EoS of Akmal, Pandharipande, and Ravenhall [36], and therefore it can no longer be compared with the HF Idaho self-energies.

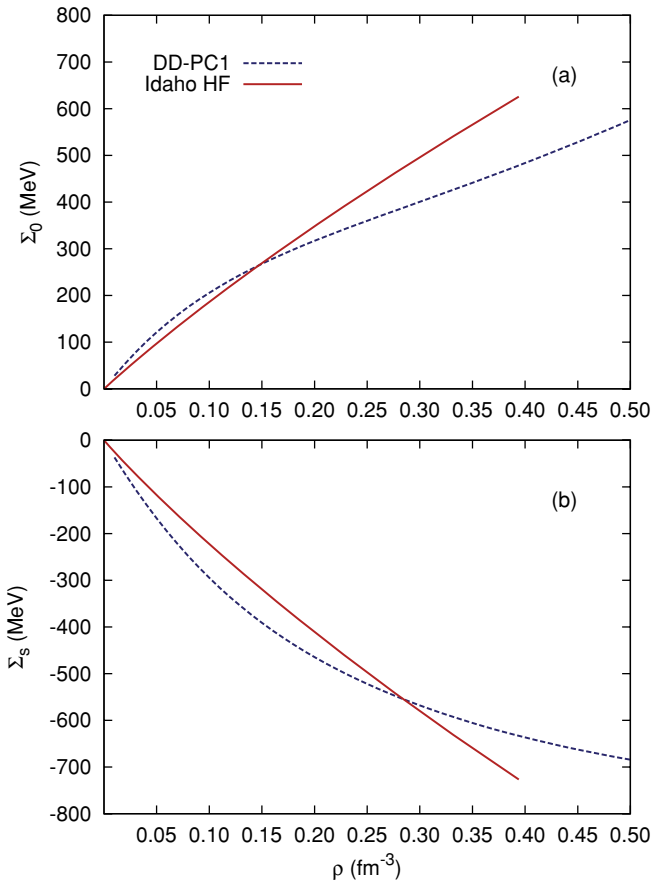

FIG. 13. (Color online) (a) Vector and (b) scalar nucleon self-energies in symmetric nuclear matter as functions of the nucleon density. The self-energies that correspond to the phenomenological density functional DD-PC1 are compared with the Hartree-Fock self-energies [33] calculated from the Idaho N^{3}LO NN potential [34].

IV. ILLUSTRATIVE CALCULATIONS

We have performed a series of test calculations of binding energies, charge isotope shifts, deformations, and isoscalar and isovector giant resonances. Ground-state properties are calculated by using the axially deformed RMF model. Pairing correlations are treated in the BCS approximation with constant pairing gaps determined from the five-point formula

$$\Delta^{(5)}(N_0) = -\frac{\Pi_{N_0}}{8}[E(N_0+2) - 4E(N_0+1) + 6E(N_0) - 4E(N_0-1) + E(N_0-2)], \quad (18)$$

where $E(N_0)$ denotes the experimental binding energy of a nucleus with N_0 neutrons (Z_0 protons) and $\Pi_{N_0} = +1(-1)$ for N_0 even (odd).

The relativistic quasiparticle random-phase approximation (RQRPA) [44,45] is used to calculate excitation energies of giant resonances in spherical nuclei. Results calculated with DD-PC1 are compared to available data, and with predictions of the meson-exchange interaction DD-ME2.

In Fig. 14 the RMF + BCS predictions for charge radii of the Nd, Sm, Gd, Dy, Er, and Yb isotopic chains are compared with data from Ref. [46]. The charge density is obtained by folding the theoretical point-proton density distribution with the Gaussian proton-charge distribution. For the latter an rms radius of 0.8 fm is used, and the resulting ground-state charge radius reads

$$r_c = \sqrt{r_p^2 + 0.64} \quad \text{fm}, \quad (19)$$

where r_p is the radius of the point-proton density distribution. Even though the two RMF interactions, meson-exchange DD-ME2 and point-coupling DD-PC1, have been adjusted by using different procedures and to different data sets, they predict virtually identical charge radii for all six isotope chains. The theoretical values are in excellent agreement with data for Nd, Sm, Gd, and Dy nuclei. For the heavier isotopes of Er and Yb, the calculated radii are only slightly

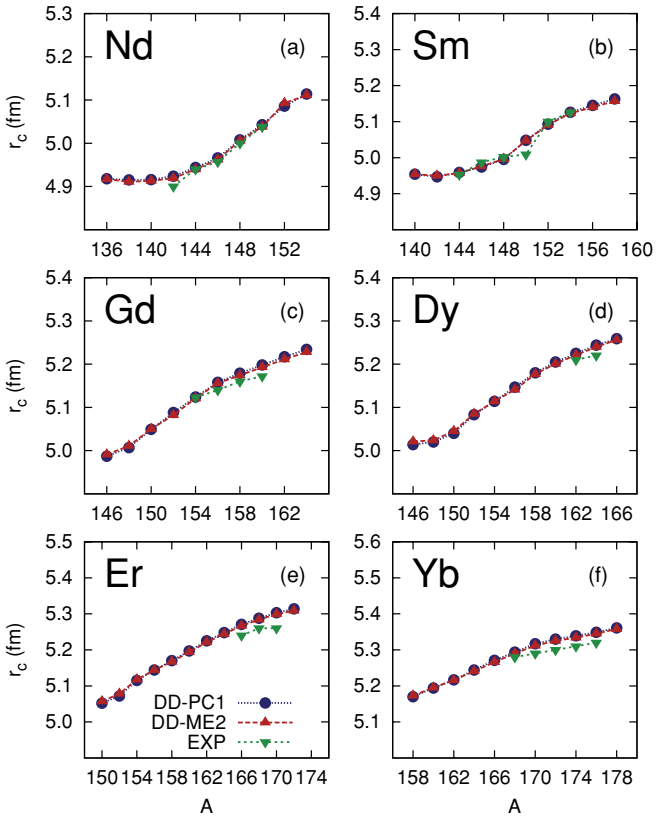

FIG. 14. (Color online) Charge radii of Nd, Sm, Gd, Dy, Er, and Yb isotopic chains. The results of the RMF + BCS calculation with the DD-PC1 and DD-ME2 interactions are compared with data [46].

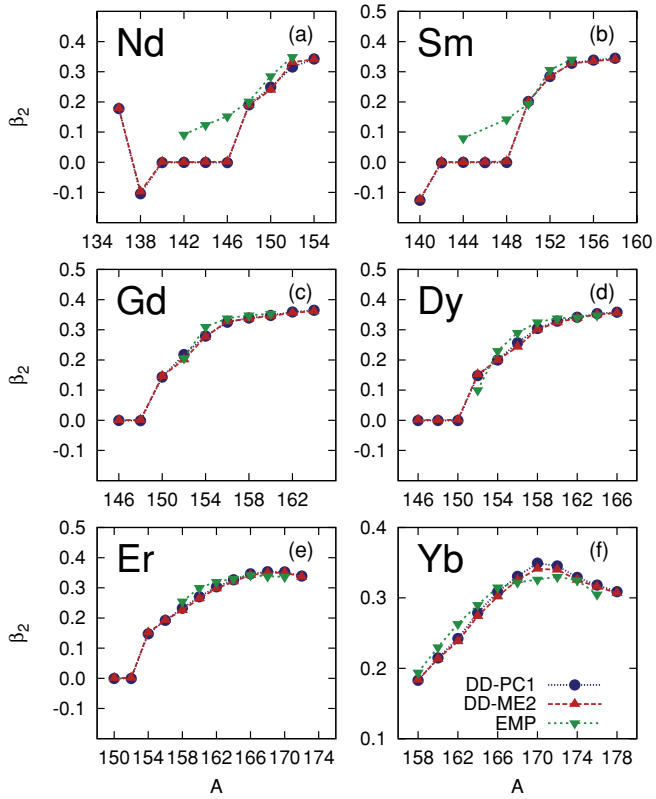

FIG. 15. (Color online) DD-PC1 and DD-ME2 predictions for the ground-state quadrupole deformations β_2 of the Nd, Sm, Gd, Dy, Er, and Yb isotopes, in comparison with empirical values [48].

above the experimental values. Note that the parameters of DD-ME2 were tuned to both binding energies and charge radii of spherical nuclei, whereas only experimental masses of deformed nuclei have been used to adjust the interaction DD-PC1. Of the nuclides that belong to the six isotopic chains shown in Fig. 14, only those with $N \geqslant 92$ are included in the data set of 64 deformed nuclei used to determine the density functional DD-PC1.

The ground-state quadrupole deformation parameters β_2 are calculated according to the prescription of Ref. [47]. The theoretical predictions for the quadrupole deformation parameters of Nd, Sm, Gd, Dy, Er, and Yb isotopes are displayed in Fig. 15, in comparison with the empirical values from Ref. [48]. Also in this case DD-ME2 and DD-PC1 predict identical ground-state shapes for all six isotopic chains and reproduce not only the global trend of the data but also the saturation of quadrupole deformation for heavier isotopes. The only discrepancy is found around the $N = 82$ closed shell in Nd and Sm isotopes, where both interactions predict spherical ground states, whereas data indicate that these nuclei are slightly prolate deformed, probably with soft potential energy surfaces. Shape coexistence structures (spherical-deformed, or prolate-oblate shapes), and soft potential surfaces in general, cannot quantitatively be described on a mean-field level. The description of coexisting shapes must include long-range correlations and necessitates angular momentum projection and configuration mixing [13,14], neither of which are considered in this work. For heavier Nd and Sm isotopes, however, the predictions of both DD-ME2 and DD-PC1 are again in excellent agreement with empirical prolate deformations.

Even though DD-PC1 is not constructed with the idea of being used as a mass formula, nevertheless this functional must also be tested in the calculation of binding energies. We consider the cases of deformed and spherical nuclei separately. As a first test Fig. 16 shows the absolute deviations of the DD-PC1 binding energies from experimental values of deformed nuclei in the mass regions $A \approx 120$–130, $A \approx 150$–180, and $A \approx 230$–250, as functions of the asymmetry coefficient and mass number. Cross symbols denote the 64 nuclei used to adjust the parameters of DD-PC1 and correspond to the deviations already shown in Fig. 7. Additional deformed nuclei that have not been used in the fit are represented by diamond symbols. We include about 20 nuclei in the mass region $A \approx 120$–130, and 12 more around mass $A \approx 150$–160. In this way the predictions for binding energies are extrapolated to a lower mass region not included in the fit and, even more importantly, to lower values of the asymmetry parameter. The overall agreement with data is very good, and the absolute deviations from experiment are contained in the interval ± 1 MeV.

In the case of spherical closed-shell nuclei, the variance between calculated masses and the corresponding experimental values is somewhat larger. This is illustrated in Fig. 17, where, for the Pb and Sn isotopic chains, we plot the absolute deviations of the calculated binding energies from

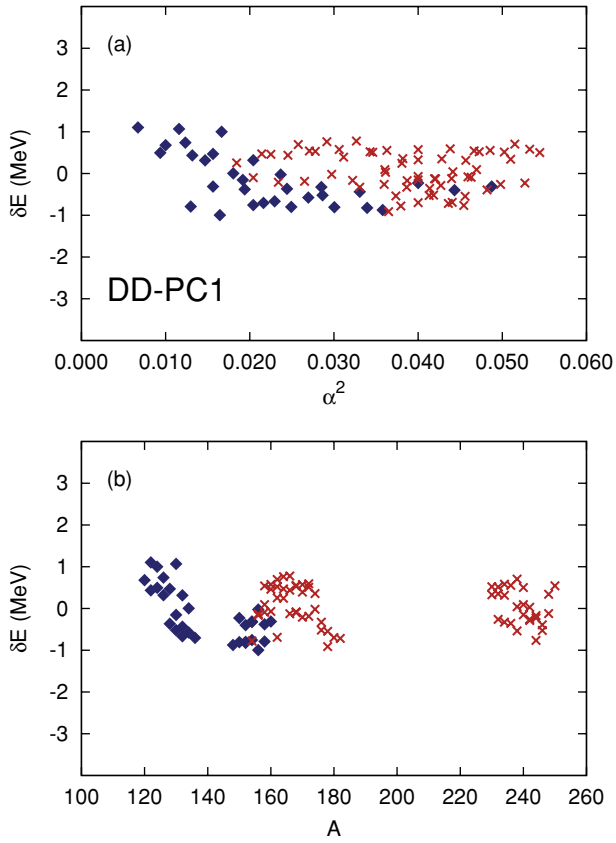

FIG. 16. (Color online) Absolute deviations of the DD-PC1 binding energies from experimental values of deformed nuclei in the mass regions $A \approx 120$–130, $A \approx 150$–180, and $A \approx 230$–250, as functions of (a) the asymmetry coefficient and (b) the mass number.

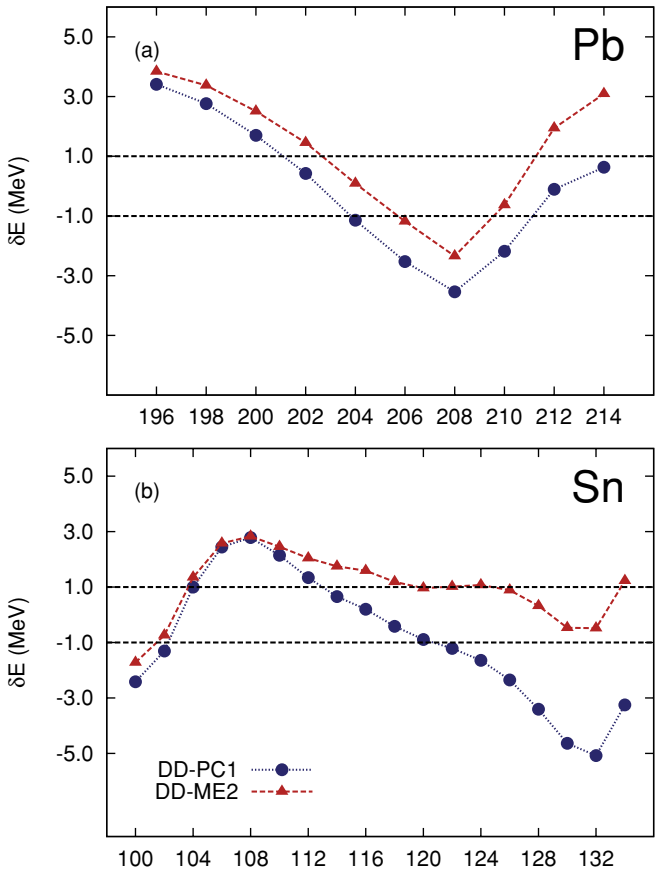

FIG. 17. (Color online) Absolute deviations of the calculated binding energies from experimental values for (a) the Pb and (b) the Sn isotopic chains, as functions of the mass number. The theoretical binding energies are calculated by using the RMF + BCS model with the point-coupling effective interaction DD-PC1 and the finite-range meson-exchange interaction DD-ME2.

data as functions of the mass number. The binding energies calculated by using the RMF + BCS model with the functional DD-PC1 are also compared to those obtained with the meson-exchange interaction DD-ME2. The latter, like most modern self-consistent mean-field nonrelativistic and relativistic interactions, was adjusted to reproduce the binding energies of doubly closed-shell nuclei, including ^{132}Sn and ^{208}Pb. In addition, of the isotopes shown in Fig. 17, the set of nuclei used to fine-tune the parameters of DD-ME2 also included ^{116}Sn, ^{124}Sn, ^{204}Pb, and ^{214}Pb. The resulting binding energies of the two isotopic chains are, of course, in better agreement with data than those predicted by the density functional DD-PC1. Because it has been tailored to masses of deformed nuclei, DD-PC1 necessarily overbinds spherical closed-shell nuclei. The situation is actually not as bad as the comparison with the experimental mass of ^{132}Sn might indicate. This isotope, with a deviation of 5.21 MeV, is in fact the worst case of those nuclei that we have calculated so far. For instance, ^{16}O is calculated to be overbound by 0.72 MeV, ^{48}Ca by 1.51 MeV, ^{208}Pb by 3.51 MeV, etc. Although the interaction DD-ME2 predicts masses of spherical nuclei closer to data, it underbinds most deformed nuclei (cf. Fig. 12).

The origin of the additional binding in closed-shell nuclei can be found in the predicted shell structure. For the two particular examples of ^{208}Pb and ^{132}Sn, this effect is illustrated in Fig. 18, which shows the comparison between experimental and DD-PC1 single-nucleon spectra of protons (upper panel) and neutrons (lower panel). The experimental spectra correspond to the single-nucleon separation energies of Ref. [49]. Note that single-nucleon orbitals are solutions of the relativistic Kohn-Sham equations and the corresponding eigenvalues, introduced just as Lagrange multipliers, do not have a directly observable physical interpretation (i.e., they cannot exactly be identified with nucleon separation energies [50]). For the last few occupied orbitals close to the Fermi surface, however, the Kohn-Sham eigenvalues approximately correspond to physical single-nucleon energies. As with most self-consistent mean-field models [1], the calculation reproduces the overall structure and ordering of single-nucleon levels, but not the level density around major shell gaps. Because of the low effective nucleon mass, the magnitude of the spherical shell gaps between occupied and unoccupied states is overestimated. As Fig. 18 clearly shows, the theoretical occupied levels are on average considerably deeper than the corresponding empirical single-nucleon states, and this effect gives rise to the overbinding that characterizes masses of spherical nuclei

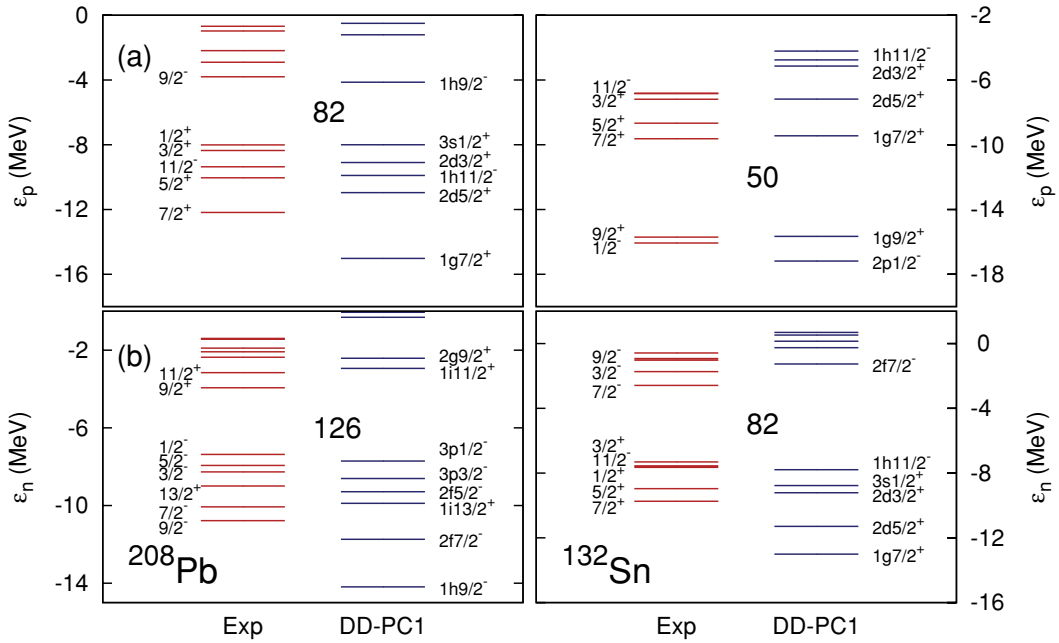

FIG. 18. (Color online) Comparison between experimental (left) and DD-PC1 (right) single-nucleon spectra of (a) protons and (b) neutrons for ^{208}Pb and ^{132}Sn. The experimental spectra are from Ref. [49].

calculated with nonrelativistic and relativistic mean-field models. We note that a similar analysis for the nonrelativistic Skyrme interaction Sly4 was carried out in Ref. [15].

This effect is particularly pronounced for the $N = 82$ neutron gap in ^{132}Sn. Not only is the theoretical gap much larger than the empirical one, but the functional DD-PC1, like many other mean-field interactions, does not reproduce the empirical sequence of neutron levels below $N = 82$. The last occupied level should be $2d_{3/2}$, whereas DD-PC1 places this orbital below $1h_{11/2}$ and $3s_{1/2}$. This increases the magnitude of the gap, and the net result is the additional binding of heavy Sn isotopes shown in Fig. 17. If an interaction with a low effective nucleon mass, such as DD-PC1 or DD-ME2, is nevertheless tuned to the masses of ^{132}Sn and ^{208}Pb, most deformed nuclei in between will be underbound, as shown for DD-ME2 in Fig. 12.

Even though it will not be considered in the present work, we would like to point out that to enhance the nonrelativistic effective (Landau) nucleon mass, the functional must go beyond the static mean-field approximation and include momentum-dependent (energy-dependent in stationary systems) nucleon self-energies. In the meson-exchange RMF framework, in particular, this has been achieved by including in the effective Lagrangian a particular form of coupling between meson fields and the derivatives of the nucleon fields [51–53]. This leads to a linear momentum dependence of the scalar and vector self-energies in the Dirac equation for the in-medium nucleon. Although this extension of the standard mean-field framework is phenomenological, it is nevertheless based on Dirac-Brueckner calculations of in-medium nucleon self-energies and consistent with the relativistic optical potential in nuclear matter, extracted from elastic proton-nucleus scattering data. In this way it was possible to increase the effective (Landau) mass to $m^*_{\rm NR} \approx 0.8m$. An additional enhancement of the effective nucleon mass in finite nuclei is caused by the coupling of single-nucleon levels to low-energy collective vibrational states [54], an effect that goes entirely beyond the mean-field approximation. In the RMF framework the coupling of single-nucleon states to low-energy phonons and the resulting increase of the effective mass were recently explored in Ref. [55].

The somewhat more pronounced deviations between the theoretical DD-PC1 and experimental masses of the Sn and Pb isotopic chains do not affect the accuracy of the calculated radii of these nuclei. In Fig. 19 the RMF + BCS model predictions for the charge radii of Pb and Sn isotopes, calculated with the effective interactions DD-PC1 and DD-ME2, are shown in comparison with empirical values [46]. The two interactions predict virtually identical values for the charge radii, in excellent agreement with data for the Sn nuclei, and only slightly above the empirical charge radii of the Pb isotopes. We note again that the charge radii of ^{116}Sn, ^{124}Sn, ^{132}Sn, ^{204}Pb, ^{208}Pb, and ^{214}Pb were used to tune the parameters of DD-ME2, whereas DD-PC1 has only been adjusted to masses. A similar result is also obtained for the thickness of the neutron skin in Pb and Sn nuclei. In Fig. 20 the DD-ME2 and DD-PC1 results for the differences between the neutron and proton rms radii are compared with available data [56–58]. Although the experimental uncertainties are large, both interactions nicely reproduce the isotopic trend of neutron radii in Sn nuclei and predict values in very good agreement with the empirical values of neutron skin thickness. These data, however, were specifically used to adjust the isovector channel of the DD-ME2 interaction, whereas in the case of DD-PC1 this level of agreement is achieved with the choice of the asymmetry energy at saturation $a_4 = 33$ MeV.

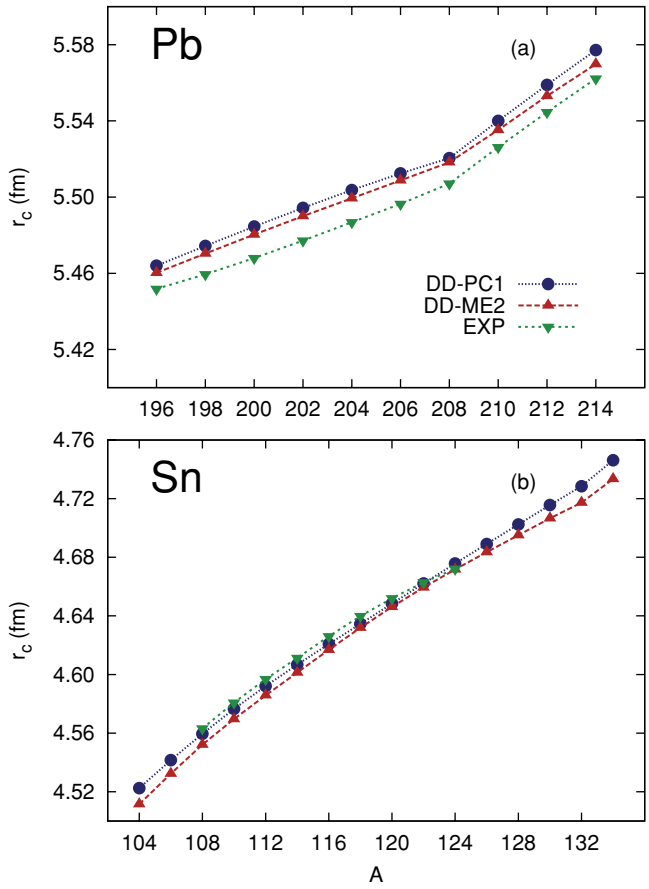

FIG. 19. (Color online) RMF + BCS model predictions for the charge radii of (a) Pb and (b) Sn isotopes, calculated with the DD-PC1 and DD-ME2 effective interactions, and compared with data [46].

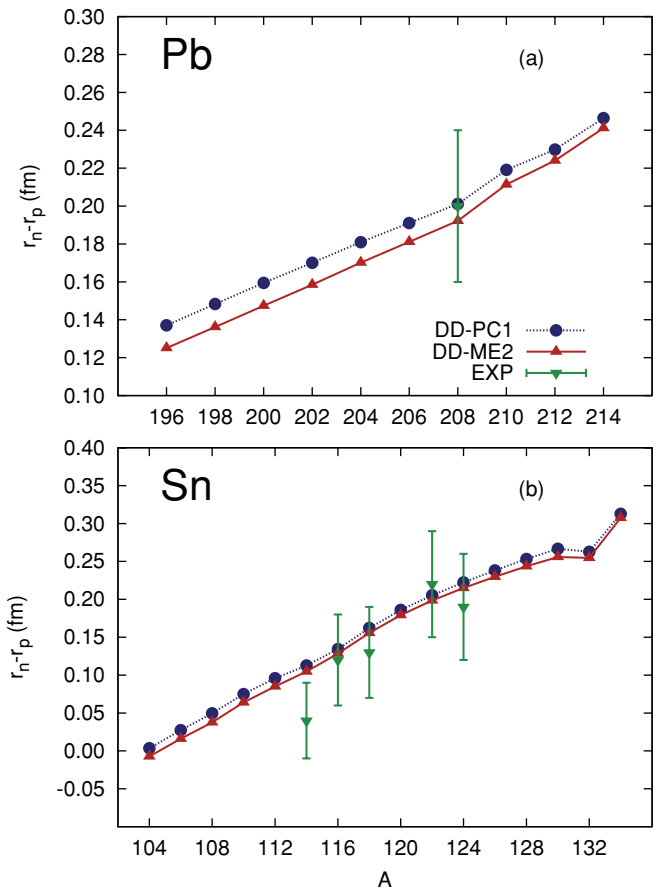

FIG. 20. (Color online) RMF + BCS model predictions for the differences between the neutron and proton rms radii of (a) Pb and (b) Sn isotopes, calculated with the DD-PC1 and DD-ME2 effective interactions, in comparison with available data [56–58].

Another very important test of self-consistent mean-field models involve excitation energies of collective modes and, in particular, giant multipole resonances. Using the relativistic (Q)RPA [44,45] with the DD-PC1 functional, we have therefore carried out a few representative calculations of giant resonances in spherical nuclei. The RQRPA is fully self-consistent; that is, in both the particle-hole and particle-particle channels the same interactions are used in the equations that determine the ground state of a nucleus and as residual interactions in the matrix equations of RQRPA. The RQRPA configuration space also includes the Dirac sea of negative energy states. In adjusting the parameters of DD-PC1 we took into account the results of Refs. [35], where it has been shown that, to reproduce the experimental excitation energies of isoscalar giant monopole resonances (ISGMR) in spherical nuclei, relativistic point-coupling interactions require a nuclear matter compression modulus of $K_{\rm nm} \approx 230$ MeV, somewhat lower than the values typically used for meson-exchange relativistic interactions [39] but within the range of values used by modern nonrelativistic Skyrme interactions. In Ref. [39] it was also shown that data on the isovector giant dipole resonance (IVGDR) constrain the range of the nuclear matter symmetry energy at saturation to $31 \leqslant a_4 \leqslant 35$ MeV, and in this work we have used $a_4 = 33$ MeV for all point-coupling interactions. For ^{208}Pb the RRPA results for the isoscalar monopole and isovector dipole response are shown in Fig. 21. For the multipole operator $\hat{Q}_{\lambda\mu}$ the response function $R(E)$ is defined as

$$R(E) = \sum_i B(\lambda_i \to 0) \frac{\Gamma/2\pi}{(E - E_i)^2 + \Gamma^2/4}, \qquad (20)$$

where $|0\rangle$ denotes the ground state of an even-even nucleus, $|\lambda_i\rangle$ is the corresponding ith excited state of multipolarity λ, Γ is the width of the Lorentzian distribution, and

$$B(\lambda \to 0) = \frac{1}{2\lambda + 1} |\langle 0||\hat{Q}_\lambda||\lambda\rangle|^2. \qquad (21)$$

The kth moment of the strength function is defined by

$$m_k(\hat{Q}_\lambda) = \sum_i E_i^k |\langle \lambda_i|\hat{Q}_\lambda|0\rangle|^2. \qquad (22)$$

The ratio m_1/m_0 is the quantity often compared with the experimental excitation energy of the corresponding resonance, although, of course, this is strictly correct only if there are no pronounced multiple peaks within the energy interval over which the summation in Eq. (22) is performed. In the examples considered here the continuous strength distributions are obtained by folding the discrete spectrum of R(Q)RPA

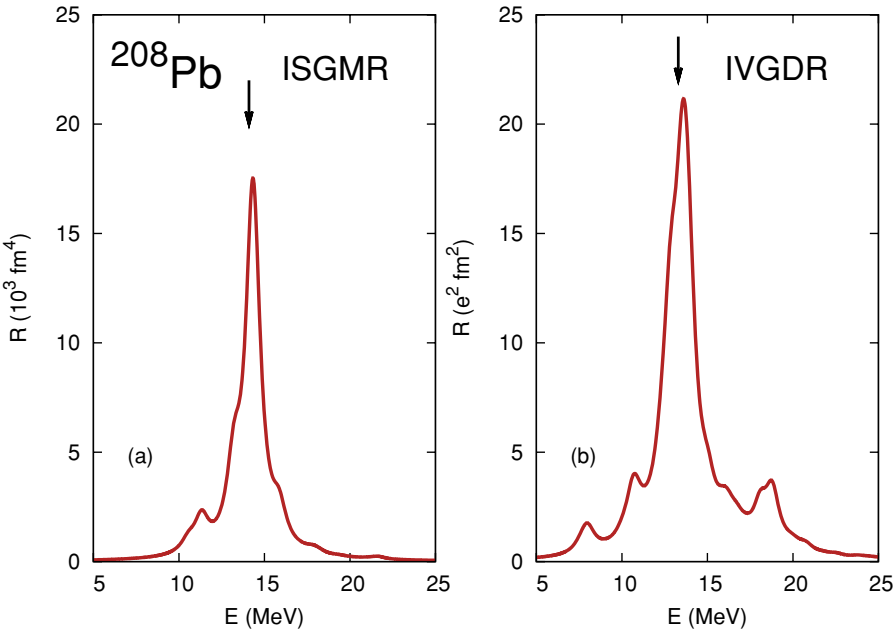

FIG. 21. (Color online) (a) Isoscalar monopole and (b) isovector dipole strength distributions in ^{208}Pb calculated with the relativistic RPA by using the effective interaction DD-PC1. The experimental excitation energies are denoted by arrows: 13.96 ± 0.2 [59] for the giant monopole resonance and 13.3 ± 0.1 [60] for the giant dipole resonance, respectively.

states with the Lorentzian [cf. Eq. (20)] of constant width $\Gamma = 1$ MeV.

The calculated excitation energies of the giant resonances in ^{208}Pb can be compared with very accurate data. For the ISGMR the calculated $m_1/m_0 = 14.17$ MeV is rather close to the experimental value $m_1/m_0 = 13.96 \pm 0.2$ MeV [59]. The relativistic RPA peak energy of the IVGDR at 13.6 MeV is also in very good agreement with the experimental excitation energy $E^* = 13.3 \pm 0.1$ MeV [60]. A similar level of agreement, both for ISGMR and IVGDR, is also obtained with the DD-ME2 interaction; however, we note that these data were taken into account in adjusting the parameters of DD-ME2 [30].

In Fig. 22 the RQRPA results for the Sn isotopes are compared with data on IVGDR excitation energies [61]. In contrast to the case of ^{208}Pb, the strength distributions in the region of giant resonances exhibit considerable fragmentation. Note, however, that the RQRPA calculation with the DD-PC1 interaction reproduces the isotopic dependence of the IVGDR and the experimental excitation energies. The theoretical peak energies 15.56 MeV (^{116}Sn), 15.35 MeV (^{118}Sn), 15.26 MeV (^{120}Sn), and 15.13 MeV (^{124}Sn) are in excellent agreement with the experimental values of 15.68 MeV (^{116}Sn), 15.59 MeV (^{118}Sn), 15.36 MeV (^{120}Sn), and 15.19 MeV (^{124}Sn), respectively.

Finally, in Fig. 23 we display the RQRPA isoscalar monopole strength functions for the chain of even-even Sn isotopes, $^{112-124}$Sn. The evolution of ISGMR in Sn isotopes can be compared with very recent data from Ref. [62]. In general, the theoretical excitation energies $E_0 = m_1/m_0$,

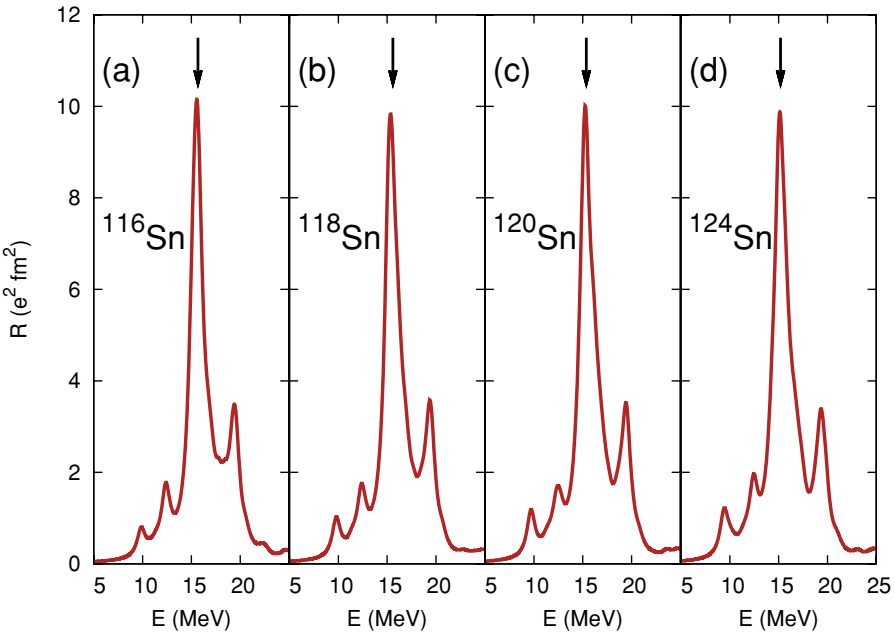

FIG. 22. (Color online) The RQRPA isovector dipole strength functions in ^{116,118,120,124}Sn, calculated with the DDPC1 effective interaction. The experimental IVGDR excitation energies [61] are denoted by arrows.

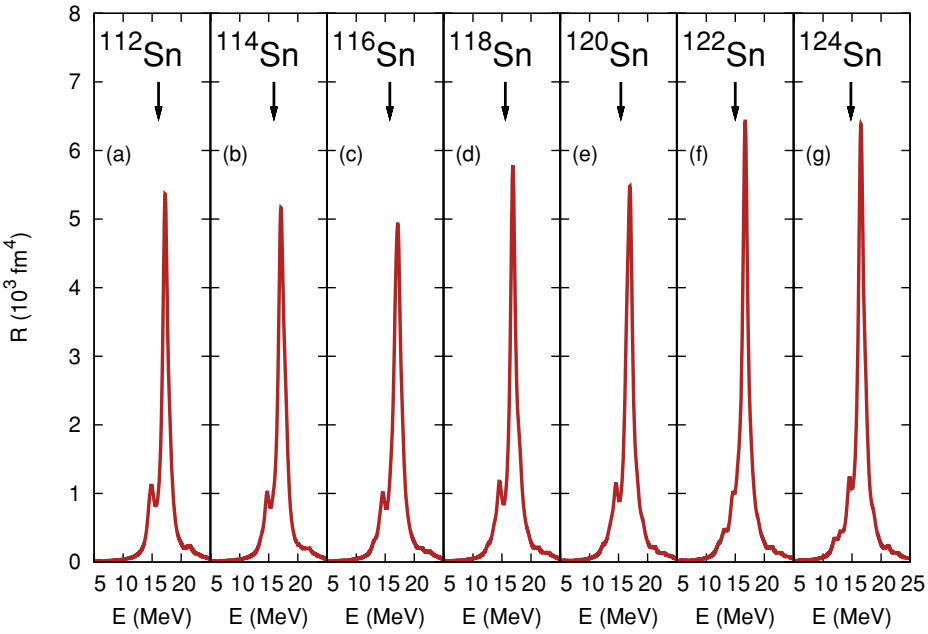

FIG. 23. (Color online) The RQRPA isoscalar monopole strength distributions in even-even $^{112-124}$Sn nuclei, calculated with the DDPC1 effective interaction. Arrows denote the positions of experimental ISGMR excitation energies [62].

when compared with the corresponding experimental values evaluated in the energy interval between 10.5 and 20.5 MeV, are systematically between 0.8 and 1 MeV higher. This result might indicate that the value of the nuclear matter compression modulus for this functional could actually be chosen as $K_{\rm nm} < 230$ MeV. However, Sn isotopes are much lighter than ^{208}Pb, and one can expect that the calculated ISGMR will be more affected by the surface incompressibility, a quantity that we have not attempted to determine in this work.

V. SUMMARY AND CONCLUDING REMARKS

The principal goal of modern nuclear structure theory is to build a consistent microscopic framework that will describe ground-state properties, nuclear excitations, and reactions at a level of accuracy comparable with experimental results and provide reliable predictions for systems very far from stability, including data for astrophysical applications that are not accessible in experiments. At present the only viable approach to a comprehensive description of arbitrarily heavy nuclear systems, including vast regions of short-lived nuclei with extreme isospin values and extended nucleonic matter, is the one based on nuclear energy density functionals.

In this work we have explored a particular class of relativistic nuclear energy density functionals in which only nucleon degrees of freedom are explicitly used in the construction of effective interaction terms. Short-distance correlations, as well as intermediate- and long-range dynamics, are effectively taken into account in the nucleon density dependence of the strength functionals of second-order contact interactions in an effective Lagrangian. By starting from microscopic nucleon self-energies in nuclear matter, a phenomenological ansatz for the density-dependent coupling functionals has been formulated and the corresponding parameters adjusted in self-consistent mean-field calculations of masses of 64 axially deformed nuclei in the mass regions $A \approx 150$–180 and $A \approx 230$–250.

The relationship between global properties of the nuclear matter equation of state and the corresponding predictions for nuclear masses has been analyzed in detail. Ground states of deformed nuclei have been calculated in the self-consistent mean-field approximation by employing sets of effective interactions with different values of the volume energy a_v, surface energy a_s, and symmetry energy a_4 in nuclear matter, whereas empirical constraints have been used for the nuclear matter saturation density, compression modulus, and Dirac effective mass. The calculated masses are not particularly sensitive to the saturation density, and previous relativistic RPA calculations of excitation energies of isoscalar giant monopole and isovector giant dipole resonances in finite nuclei, as well as results for the neutron skin thickness, have been used to determine the nuclear matter compression modulus and symmetry energy, respectively.

One of the important results of the careful analysis of deviations between calculated and experimental masses (mass residuals) is the pronounced isospin and mass dependence of the residuals on the nuclear matter volume energy at saturation. To reduce the absolute mass residuals to less than 1 MeV, and to contain their mass and isotopic dependence, strict constraints on the value of a_v must be met. The narrow window of allowed values of the volume energy cannot be determined microscopically already at the nuclear matter level; rather, it results from a fine-tuning of the parameters of the energy density functional to experimental masses. Calculated binding energies and charge radii are also sensitive to the choice of the surface coefficient a_s that determines the surface energy and surface thickness of semi-infinite nuclear matter. In the functional considered in the present work, these quantities are controlled by the strength of the derivative isoscalar-scalar coupling interaction. The range of allowed values of the strength parameter determined by data is in very

good agreement with estimates obtained from microscopic calculations of inhomogeneous nuclear matter.

The optimal energy density functional (DD-PC1) determined in a multistep parameter fit to the masses of 64 axially deformed nuclei has been further tested in calculations of properties of spherical and deformed medium-heavy and heavy nuclei, including binding energies, charge radii, deformation parameters, neutron skin thickness, and excitation energies of giant multipole resonances. Results have been compared with available data, and with predictions of one of the most successful finite-range meson-exchange relativistic effective interactions: DD-ME2. In general, a very good agreement with data has been obtained except, perhaps, for the effect of overbinding of spherical closed-shell nuclei. DD-PC1, like virtually all relativistic mean-field models, is characterized by a relatively low effective nucleon mass and, when adjusted to masses of deformed nuclei, it overbinds spherical closed-shell systems. The well-known problem of arches of mass residuals between shell closures could be addressed by a functional that goes beyond the static mean-field approximation, but this approach has not been considered in the present model. Very good results have been obtained for the excitation energies of giant monopole and dipole resonances in spherical nuclei, calculated with the relativistic quasiparticle random-phase approximation based on the DD-PC1 functional. The agreement with data confirms the choice of the nuclear matter compressibility and symmetry energy for DD-PC1.

The total number of parameters in the functional DD-PC1 is 10, as in most nonrelativistic Skyrme-type density functionals. Note, however, that the effective Lagrangian of DD-PC1 contains only four interaction terms except, of course, the Coulomb term [cf. Eq. (2)]. The 10 parameters determine the density dependence of the strength functionals and reflect the complex nuclear many-body dynamics. We also emphasize that, because the high-density behavior of the corresponding nuclear matter EoS has been adjusted to a microscopic EoS extensively used in studies of high-density nucleon matter and neutron stars, DD-PC1 should also be tested in astrophysical applications.

This work is part of a program to develop an universal relativistic energy density functional to be used in studies of the evolution of shell structure, deformation, shape coexistence phenomena, rotational bands, etc. in transitional and deformed nuclei. In the first step the parameters of the density functional have been adjusted to reproduce binding energies of a large set of axially deformed nuclei. In the continuation of this program we plan to build a functional, based on DD-PC1, to be used in the new relativistic model that employs the generator coordinate method (GCM) to perform configuration mixing of angular-momentum and particle-number projected mean-field wave functions. However, if rotational energy corrections and quadrupole fluctuations are treated explicitly in the GCM framework, they should not at the same time implicitly be included in the functional (i.e., through parameters adjusted to data that already include correlations). Therefore, starting from DD-PC1, the parameters of this new functional can be adjusted to pseudodata, obtained by subtracting correlation effects from experimental masses and radii. The resulting energy density functional will be tested in relativistic GCM model studies of shell evolution, deformations, shape coexistence, and shape phase transitions.

ACKNOWLEDGMENTS

We thank O. Plohl and C. Fuchs for providing the Hartree-Fock nucleon self-energies based on the Idaho N^3LO NN potential. This work was supported in part by MZOS Project No. 1191005-1010 and by the DFG cluster of excellence "Origin and Structure of the Universe" (www.universe-cluster.de).

[1] M. Bender, P.-H. Heenen, and P.-G. Reinhard, Rev. Mod. Phys. **75**, 121 (2003).
[2] D. Vretenar, A. V. Afanasjev, G. A. Lalazissis, and P. Ring, Phys. Rep. **409**, 101 (2005).
[3] W. Kohn and L. J. Sham, Phys. Rev. **140**, A1133 (1965).
[4] W. Kohn, Rev. Mod. Phys. **71**, 1253 (1999).
[5] G. A. Lalazissis, P. Ring, and D. Vretenar, edited by, *Extended Density Functionals in Nuclear Structure Physics* (Springer-Verlag, Heidelberg, 2004), Lecture Notes in Physics Vol. 641.
[6] B. D. Serot and J. D. Walecka, Adv. Nucl. Phys. **16**, 1 (1986).
[7] B. D. Serot and J. D. Walecka, Int. J. Mod. Phys. E **6**, 515 (1997).
[8] R. J. Furnstahl and B. D. Serot, Comments Nucl. Part. Phys. **2**, A23 (2000).
[9] J. N. Ginocchio, Phys. Rep. **414**, 165 (2005).
[10] P. Finelli, N. Kaiser, D. Vretenar, and W. Weise, Nucl. Phys. **A735**, 449 (2004).
[11] P. Finelli, N. Kaiser, D. Vretenar, and W. Weise, Nucl. Phys. **A770**, 1 (2006).
[12] S. Fritsch, N. Kaiser, and W. Weise, Nucl. Phys. **A750**, 259 (2005).
[13] T. Nikšić, D. Vretenar, and P. Ring, Phys. Rev. C **73**, 034308 (2006).
[14] T. Nikšić, D. Vretenar, and P. Ring, Phys. Rev. C **74**, 064309 (2006).
[15] M. Bender, G. F. Bertsch, and P.-H. Heenen, Phys. Rev. C **73**, 034322 (2006).
[16] M. Bender, G. F. Bertsch, and P.-H. Heenen, Phys. Rev. C **69**, 034340 (2004).
[17] M. Bender, P. Bonche, and P.-H. Heenen, Phys. Rev. C **74**, 024312 (2006).
[18] E. Clément *et al.*, Phys. Rev. C **75**, 054313 (2007).
[19] T. Nikšić, D. Vretenar, G. A. Lalazissis, and P. Ring, Phys. Rev. Lett. **99**, 092502 (2007).
[20] B. A. Nikolaus, T. Hoch, and D. G. Madland, Phys. Rev. C **46**, 1757 (1992).
[21] T. Hoch, D. Madland, P. Manakos, T. Mannel, B. A. Nikolaus, and D. Strottman, Phys. Rep. **242**, 253 (1994).
[22] J. L. Friar, D. G. Madland, and B. W. Lynn, Phys. Rev. C **53**, 3085 (1996).
[23] J. J. Rusnak and R. J. Furnstahl, Nucl. Phys. **A627**, 495 (1997).
[24] T. Bürvenich, D. G. Madland, J. A. Maruhn, and P.-G. Reinhard, Phys. Rev. C **65**, 044308 (2002).
[25] F. Hofmann, C. M. Keil, and H. Lenske, Phys. Rev. C **64**, 034314 (2001).

[26] S. Typel and H. H. Wolter, Nucl. Phys. **A656**, 331 (1999).
[27] T. Nikšić, D. Vretenar, P. Finelli, and P. Ring, Phys. Rev. C **66**, 024306 (2002).
[28] C. Fuchs, H. Lenske, and H. H. Wolter, Phys. Rev. C **52**, 3043 (1995).
[29] F. de Jong and H. Lenske, Phys. Rev. C **57**, 3099 (1998).
[30] G. A. Lalazissis, T. Nikšić, D. Vretenar, and P. Ring, Phys. Rev. C **71**, 024312 (2005).
[31] W. Long, J. Meng, N. Van Giai, and S.-G. Zhou, Phys. Rev. C **69**, 034319 (2004).
[32] W. Long, N. Van Giai, and J. Meng, Phys. Lett. **B640**, 150 (2006).
[33] O. Plohl and C. Fuchs, Phys. Rev. C **74**, 034325 (2006).
[34] D. R. Entem and R. Machleidt, Phys. Rev. C **68**, 041001(R) (2003).
[35] T. Nikšić, D. Vretenar, G. A. Lalazissis, and P. Ring, Phys. Rev. C **77**, 034302 (2008).
[36] A. Akmal, V. R. Pandharipande, and D. G. Ravenhall, Phys. Rev. C **58**, 1804 (1998).
[37] G. F. Bertsch, B. Sabbey, and M. Uusnäkki, Phys. Rev. C **71**, 054311 (2005).
[38] R. J. Furnstahl, Nucl. Phys. **A706**, 85 (2002).
[39] D. Vretenar, T. Nikšić, and P. Ring, Phys. Rev. C **68**, 024310 (2003).
[40] D. Hofer and W. Stocker, Nucl. Phys. **A492**, 637 (1989).
[41] P. Ring, Y. K. Gambhir, and G. A. Lalazissis, Comput. Phys. Commun. **105**, 77 (1997).
[42] G. Audi, A. H. Wapstra, and C. Thibault, Nucl. Phys. **A729**, 337 (2003).
[43] E. N. E. van Dalen, C. Fuchs, and A. Faessler, Phys. Rev. Lett. **95**, 022302 (2005).
[44] N. Paar, P. Ring, T. Nikšić, and D. Vretenar, Phys. Rev. C **67**, 034312 (2003).
[45] T. Nikšić, D. Vretenar, and P. Ring, Phys. Rev. C **72**, 014312 (2005).
[46] E. G. Nadjakov, K. P. Marinova, and Yu. P. Gangrsky, At. Data Nucl. Data Tables **56**, 133 (1994).
[47] J. Libert and P. Quentin, Phys. Rev. C **25**, 571 (1982).
[48] S. Raman, C. Nestor, and P. Tikkanen, At. Data Nucl. Data Tables **78**, 1 (2001).
[49] V. I. Isakov, K. I. Erokhina, H. Mach, M. Sanchez-Vega, and B. Fogelberg, Eur. Phys. J. A **14**, 29 (2002).
[50] R. M. Dreizler and E. K. U. Gross, *Density Functional Theory* (Spinger-Verlag, Berlin, 1990).
[51] S. Typel, T. V. Chossy, and H. H. Wolter, Phys. Rev. C **67**, 034002 (2003).
[52] S. Typel, Phys. Rev. C **71**, 064301 (2005).
[53] T. Marketin, D. Vretenar, and P. Ring, Phys. Rev. C **75**, 024304 (2007).
[54] C. Mahaux, P. F. Bortignon, R. A. Broglia, and C. H. Dasso, Phys. Rep. **120**, 1 (1985).
[55] E. Litvinova and P. Ring, Phys. Rev. C **73**, 044328 (2006).
[56] A. Krasznahorkay *et al*., Phys. Rev. Lett. **82**, 3216 (1999).
[57] V. E. Starodubsky and N. M. Hintz, Phys. Rev. C **49**, 2118 (1994).
[58] A. Krasznahorkay *et al*., Nucl. Phys. **A567**, 521 (1994).
[59] D. H. Youngblood, Y.-W. Lui, H. L. Clark, B. John, Y. Tokimoto, and X. Chen, Phys. Rev. C **69**, 034315 (2004).
[60] J. Ritman *et al*., Phys. Rev. Lett. **70**, 533 (1993).
[61] B. L. Berman and S. C. Fultz, Rev. Mod. Phys. **47**, 713 (1975).
[62] T. Li *et al*., Phys. Rev. Lett. **99**, 162503 (2007).